PERFORMANCE CHARACTERISTICS OF LIQUID METAL HEAT PIPE IN A TRANSVERSE MAGNETIC FIELD

Yoshiharu FUKUZAWA

PERFORMANCE CHARACTERISTICS OF LIQUID METAL HEAT PIPE IN A TRANSVERSE MAGNETIC FIELD

(垂直磁場中での液体金属ヒートパイプの作動特性)

Doctor Thesis

by

Yoshiharu FUKUZAWA

Department of Nuclear Engineering

Faculty of Engineering

Osaka University

Osaka

Japan

1980

Nomenclature

A	Cross sectional area
B	Magnetic field strength
M	Mass flow rate
P	Pressure
Q	Heat transport rate
T	Temperature
V	Volume
g	Acceleration of gravity
l	Axial length
r	Radius
v	Velocity
z	Position
λ	Latent heat
μ	Viscosity
ρ	Density
σ	Electrical conductivity
ψ	Angle of inclination

Subscripts

a Adiabatic section

b Magnetic field

c Condenser section

e Evaporator section

ℓ Liquid

v Vapor

Contents

Chapter 1.

Introduction

A heat pipe is defined as a closed structure including a working fluid which transports thermal energy from one part of the structure to another one by means of vaporization of the liquid, transport and condensation of the vapor, and the subsequent return of the condensate due to capillary action from the condenser to the evaporator section through a porous material called the wick. Since Grover et al.[1] at Los Alamos Scientific Laboratory reported its high heat transport capability in 1964, heat pipe study has steadily advanced in keeping with the growing interest.

The research field of the heat pipe is divided into the basic and the applied ones. In the applied research field, Werner[2] has proposed to use the heat pipes for power flattening in the controlled thermonuclear reactor (CTR) blanket. In this application, liquid metals such as potassium and sodium will be used as the working fluid because of its high operating temperature. The liquid metal has a high electrical conductivity, and there is a strong magnetic field for plasma confinement in the blanket. Then the liquid flow in the wick suffers from the magnetohydrodynamic (MHD) effect within the blanket and the performance characteristics of the heat pipe would be influenced by the MHD effect.

The basic research field is divided into the study of heat transport limits and that of heat transport characteristics at various operating conditions. The heat transport rate of the

heat pipe is limited by four factors ; the sonic vapor flow, the liquid entrainment, the pumping ability due to capillary action and the boiling in the evaporator wick. The limiting curves of these four types are schematically shown in Fig.1-1, which describes the relation between the heat transport rate and the vapor temperature. The sonic limiting curve represents an ultimate limit which cannot be exceeded regardless of the wick structure, whereas the other limits depend on the wick design. An analytical model for the sonic limit was proposed by Levy[3], and subsequently Kemme[4] performed the experiment. The entrainment limit depends on the characteristics of the wick surface. Kemme[5] studied also on this limit and experimentally showed that the heat transport rate was improved by covering the wick surface with a layer of fine mesh screen. The heat transport rate limit due to the maximum wick pumping pressure has been studied by several investigators. This limit depends on the wick structure and on the angle of inclination of the heat pipe in the gravitational field. Boiling in the wick interrupts the liquid supply to the evaporator section and leads the heat pipe operation to failure.

The operating region of the heat pipe is the area enclosed by these four limiting curves and the abscissa in Fig. 1-1. The heat transport characteristics of the heat pipe within this area can be considered to be influenced by the following factors ;

(1) the non-condensable gas inclusion, (2) the vapor flow resistance, and (3) the liquid flow resistance. The influence of these factors on the heat transport characteristics are studied from the viewpoint of the control of the heat transport rate and/or the operating temperature of the heat pipe. The influence of non-condensable gas has been studied by Marcus et al.[6] for the low temperature heat pipes with water, ammonia and methanol as working fluid from the viewpoint of the application to spacecraft thermal control. The control techniques which deal with the factors (2) and (3) are called "vapor flow control" and "liquid flow control", respectively. In these flow controls, a throttle nozzle or a valve is used for interrupting or throttling the flow between the evaporator and the condenser sections. As for the liquid metal heat pipe, a transverse magnetic field can be considered to be useful for the liquid flow control, since the liquid flow suffers from the MHD effect.

The present thesis covers the study of the performance characteristics of the liquid metal heat pipe in the magnetic field. The discussions deal with heat transport limits except entrainment and with heat transport characteristics in the magnetic field. In addition, the discussions deal also with the influence of non-condensable gas on the heat transport characteristics, because the liquid metal heat pipe is liable to be mixed with gaseous impurities due to the high operating temperature and then the heat transport characteristics would be influenced by the gas.

These items affect the feasibility of liquid flow control by the magnetic field and have implications on the heat pipe application to the CTR blanket.

In Chapter 2, the heat transport equation of the heat pipe in the magnetic field is formularized for discussion in the following chapters from the viewpoint of liquid flow in the wick.

In Chapter 3, the influence of the magnetic field existing in the adiabatic section on heat transport characteristics of potassium heat pipe is discussed with reference to the heat transport rate and the operating temperature.

In Chapter 4, the influence of the magnetic field on the wick pumping limit is dealt with.

In Chapter 5, the influence of the magnetic field on the boiling limit is discussed from the viewpoint of the incipient boiling superheat of liquid in the magnetic field.

In Chapter 6, the influence of non-condensable gas on the heat transport characteristics is dealt with, for a further discussion of the experimental results described in Chapter 3. The influence of the gravitational force on heat transport characteristics is also discussed over a wide range of gas loaded.

Finally, the summary conclusions are described in Chapter 7.

References

(1) Grover, G. M., Cotter, T. P. and Erickson, G. F. : J. Appl. Phys. 35 (1964).

(2) Werner, R. W. : B.N.E.S. Nuclear Fusion Reactor Conf. at Culham Lab. (Sept. 1969).

(3) Levy, E. K. : J. Eng. for Industry, Trans. ASME (Nov. 1968).

(4) Kemme, J. E. : IEEE Transactions on Electron Devices, Vol. ED-16, No. 8 (Aug. 1969).

(5) Kemme, J. E. : IEEE Conf. Record (1967).

(6) Marcus, B. D. : NASA CR-2018 (1972).

(7) Winter, E. R. F. and Barsch, W. O. : Advances in Heat Transfer, Vol.7, p219 (1971).

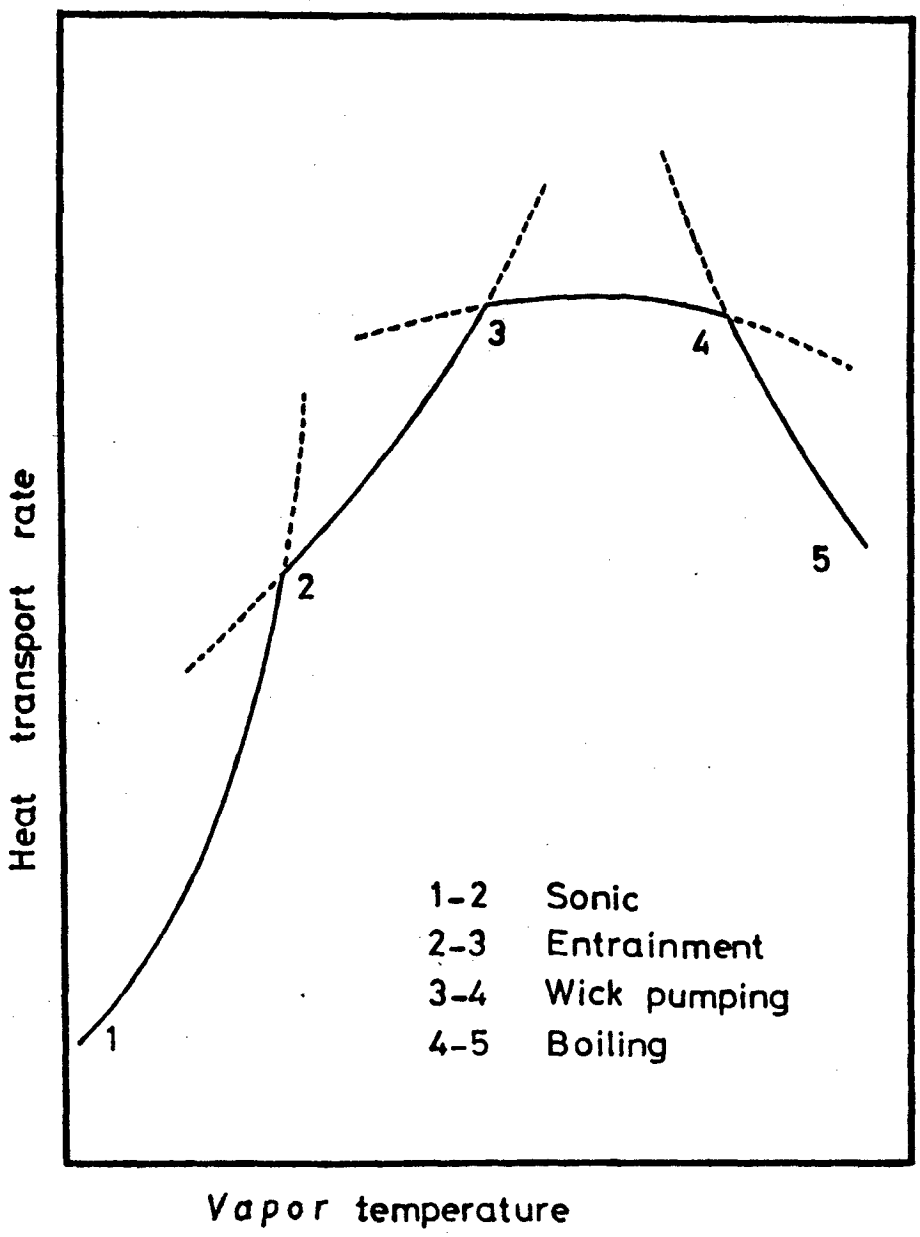

Fig.1-1 Limits to heat pipe operation

Chapter 2.

Formulation

2-1 Introduction

The pressure distribution in the heat pipe is schematically shown in Fig. 2-1, where ΔP_{vo} and $\Delta P_{\ell o}$ are the pressure differences between both ends of the heat pipe in the vapor flow and the liquid one, respectively, and ΔP_{cap} and $\Delta P'_{cap}$ are the pressure differences between the vapor and the liquid in the evaporator and the condenser sections, respectively. Usually $\Delta P'_{cap}$ is very small. Then the pressure balance in the heat pipe is expressed as follows ($\Delta P'_{cap} \equiv 0$):

$$\Delta P_{cap} = \Delta P_{vo} + \Delta P_{\ell o}. \qquad (2\text{-}1)$$

The body forces acting on the vapor flow such as magnetic force or gravitational one are small enough to be negligible. Then the heat transport rate obtained from the viewpoint of the vapor flow is expressed as follows ;(1)

$$Q = \frac{2\lambda A_v}{\sqrt{\pi^2-4}} \cdot \sqrt{\rho_v \cdot \Delta P_{vo}}, \qquad (2\text{-}2)$$

where λ is the latent heat for evaporation, ρ_v is the vapor density and A_v is the vapor flow area in the heat pipe.

On the other hand, liquid flow in the wick is generally described by Darcy's law and then the heat transport rate in the zero magnetic field is expressed as follows ;(2)

$$Q = \frac{\lambda \rho_\ell K_\ell A_{eff}}{\mu_\ell \left\{ l_a + \frac{1}{2}(l_e + l_c) \right\}} \cdot \left\{ \Delta P_{\ell o} - \rho_\ell g (l_e + l_a + l_c) \sin\psi \right\}, \qquad (2\text{-}3)$$

where K_ℓ is the permeability in Darcy's law, A_{eff} is the effective flow area for liquid in the wick, ρ_ℓ is the liquid density, μ_ℓ is the liquid viscosity, g is the acceleration of gravity, ψ is the angle of inclination and l_e, l_a and l_c are the axial lengths of the evaporator, the adiabatic and the condenser sections, respectively.

In the magnetic field, liquid flow in the wick suffers from the MHD effect. Then the heat transport equation obtained by taking account of the MHD effect in the wick is required for the discussion on the heat transport characteristics of the heat pipe in the magnetic field. In the special case of the wick structure of the grooves type which is composed of many grooves covered with a layer of mesh screen, the pressure loss due to the MHD effect could be estimated, with the unit groove having the shape of a single straight tube.[1] Usually, the heat pipe wick is composed of a porous material. In this case, the MHD effect in the wick is not studied yet since the liquid flow path is very complicated due to the porous wick structure. In this chapter, the heat transport equation of the heat pipe in the magnetic field is considered from the viewpoint of liquid flow in the wick on the basis of Darcy's law.

2-2 Darcy's Law in the Magnetic Field

The liquid flow in a porous wick of a liquid metal heat pipe can be described by Darcy's law. Then the mean axial velocity

of liquid is expressed as follows ;

$$v_\ell = -\frac{K_\ell}{\mu_\ell}\left(\frac{dP_\ell}{dz} + \rho_\ell g \sin\psi\right) , \qquad (2\text{-}4)$$

where dP_ℓ/dz is the pressure gradient in the flow direction. Relation (2-4) is a semi-empirical law by the introduction of the empirical constant K_ℓ and is regarded as an extension of Poiseuille's law.[3] In the following, Darcy's law is extended and applied to the flow in the wick under the magnetic field. From Eq.(2-4), Darcy's law is transformed to

$$-\frac{dP_\ell}{dz} = \mu_\ell \frac{v_\ell}{K_\ell} + \rho_\ell g \sin\psi \quad . \qquad (2\text{-}5)$$

In general, the effect of the magnetic field on a flow is divided into two effects : the increase of the frictional pressure loss due to the change of flow velocity distribution and the magnetic body force acting on the fluid. For the flow in the porous wick in the magnetic field, the former effect should be expressed as the change of the permeability and the latter one should be added as the magnetic pressure loss to the right-hand side of Eq.(2-5). Then the flow in the porous wick in the magnetic field can be expressed as follows ;

$$-\frac{dP_\ell}{dz} = \mu_\ell \frac{v_\ell}{K_{\ell b}} + \rho_\ell g \sin\psi + \beta \sigma_\ell v_\ell B^2 , \qquad (2\text{-}6)$$

where $K_{\ell b}$ is the permeability in the magnetic field, β is the coefficient of the magnetic pressure loss, σ_ℓ is the electrical conductivity of liquid and B is the magnetic field strength. Equation (2-6) can be arranged to

$$-\frac{dP_\ell}{dz} = \mu_\ell \frac{v_\ell}{K_\ell} + \rho_\ell g \sin\psi + \mu_\ell \frac{v_\ell}{K_\ell} \cdot \frac{K_\ell - K_{\ell b}}{K_{\ell b}} + \beta \sigma_\ell v_\ell B^2 \quad . \tag{2-7}$$

The third term in the right-hand side of Eq.(2-7) represents the increase of the frictional pressure loss due to the change of the permeability and the fourth term represents the magnetic pressure loss in the wick.

From Eq.(2-7), the mean axial velocity in the magnetic field is obtained as follows ;

$$v_\ell = -\frac{1}{1 + \frac{K_\ell - K_{\ell b}}{K_{\ell b}} + \beta Ha^2} \cdot \frac{K_\ell}{\mu_\ell} \left(\frac{dP_\ell}{dz} + \rho_\ell g \sin\psi\right) , \tag{2-8}$$

where $Ha \equiv \sqrt{\sigma_\ell B^2 K_\ell / \mu_\ell}$. (2-9)

Equation (2-8) includes the two effects of the magnetic field and agrees with Eq.(2-4) when B = 0. Equation (2-8) can be regarded as the general expression of Darcy's law in the magnetic field. In addition, Ha defined in Eq.(2-9) is considered as a "Hartmann number" of the flow in the wick, since the Hartmann number is defined by the root of the ratio of the magnetic force to the viscous one.

2-3 Flow Resistance in the Wick

Let us now deal with the flow resistance of liquid in the wick under the magnetic field. The magnetic field is assumed to be applied perpendicularly to the portion of the adiabatic section of the heat pipe.

In the adiabatic section, the mass flow rate of liquid in the wick is

$$M_\ell = \rho_\ell v_\ell A_{eff} \quad . \tag{2-10}$$

By approximating dP_ℓ/dz in Eq.(2-8) to $-\Delta P_\ell / \Delta z$, and using $\Delta P_{\ell b}$ for ΔP_ℓ and l_b for Δz, the mass flow rate in the portion of the adiabatic section, where the magnetic field is present, is obtained from Eqs.(2-8) and (2-10) as follows ;

$$M_\ell = \frac{1}{1+\frac{K_\ell - K_{\ell b}}{K_{\ell b}}+\beta Ha^2} \cdot \frac{\rho_\ell K_\ell A_{eff}}{\mu_\ell l_b} (\Delta P_{\ell b} - \rho_\ell g l_b \sin\psi) \quad , \tag{2-11}$$

where l_b is the axial length of the magnetic field and $\Delta P_{\ell b}$ is the pressure drop in the magnetic field. In the other region of the adiabatic section where the magnetic field is absent, the mass flow rate is

$$M_\ell = \frac{\rho_\ell K_\ell A_{eff}}{\mu_\ell (l_{a-b})} \left\{ \Delta P_{\ell(a-b)} - \rho_\ell g (l_{a-b}) \sin\psi \right\} \quad , \tag{2-12}$$

where $\Delta P_{\ell(a-b)}$ is the pressure drop in this region (see Fig.2-1). In the evaporator and the condenser sections where the mass flow rate changes along the axial direction, the whole

evaporation and condensation rates ($=M_\ell'$) can be respectively expressed after the integration as follows ;[2]

$$M_\ell = \frac{2\rho_\ell K_\ell A_{eff}}{\mu_\ell l_e} (\Delta P_{\ell e} - \rho_\ell g l_e \sin\psi) , \tag{2-13}$$

$$M_\ell = \frac{2\rho_\ell K_\ell A_{eff}}{\mu_\ell l_c} (\Delta P_{\ell c} - \rho_\ell g l_c \sin\psi) , \tag{2-14}$$

where the factor 2 is based on the assumption that the distribution of the specific evaporation and the condensation rates (per unit length) in these sections is uniform.
From Eqs.(2-11) ~ (2-14), the following equation is obtained.

$$M_\ell = \{\Delta P_{\ell o} - \rho_\ell g l_o \sin\psi\}/R_\ell(B) , \tag{2-15}$$

where $\Delta P_{\ell o} \equiv \Delta P_{\ell e} + \Delta P_{\ell(a-b)} + \Delta P_{\ell b} + \Delta P_{\ell c}$, $l_o \equiv l_e + l_a + l_c$, (2-16)

and $R_\ell(B) \equiv R_{\ell o}\cdot(1+\zeta)$, (2-17)

where $R_{\ell o} \equiv \mu_\ell\{l_a + (l_e+l_c)/2\}/(\rho_\ell K_\ell A_{eff})$, (2-18)

and $\zeta \equiv \left(\frac{K_\ell - K_{\ell b}}{K_{\ell b}} + \beta Ha^2\right) \cdot \frac{l_b}{l_a + \frac{1}{2}(l_e+l_c)}$. (2-19)

The pressure difference in liquid between both ends of the heat pipe, $\Delta P_{\ell o}$, is equal to the wick pumping pressure for liquid and then the bracket in the right-hand side of Eq.(2-15) represents the wick pumping ability. The over-all flow resistance of

liquid in the wick in the absence of the magnetic field is represented by $R_{\ell o}$ and then ζ is the increasing rate of flow resistance due to the MHD effect. The MHD effect on the liquid flow can be regarded as the increase of flow resistance as shown in Eq.(2-17). Then $R_\ell(B)$ represents the effective flow resistance which includes the effect of the magnetic field on the flow.

2-4 Heat Transport Equation of the Heat Pipe

In the steady condition, the liquid mass flow rate in the axial direction is equal to the vapor rate. Then the heat transport rate can be expressed as follows ;

$$Q = \lambda M_\ell \ . \tag{2-20}$$

From Eqs.(2-15) and (2-20), the following equation is obtained.

$$Q = \lambda(\Delta P_{\ell o} - \rho_\ell g l_o \sin\psi)/R_\ell(B) \ , \tag{2-21}$$

Equation (2-21) is the heat transport equation of the heat pipe in the magnetic field, which is obtained from the viewpoint of the liquid mass flow rate in the wick on the basis of Darcy's law. As shown in Eq.(2-21), the heat transport rate in the presence of the magnetic field is expressed in terms of the latent heat for evaporation, the wick pumping pressure and the effective flow resistance which includes the effect of the magnetic field on the flow in the wick.

2-5 Concluding remarks

The MHD effect can be regarded as the increase of the flow resistance of the liquid flow in the wick. Then the heat transport rate in the presence of the magnetic field is expressed by using the term of the increasing rate of flow resistance due to the MHD effect. The increasing rate depends on the Hartmann number which is defined by $\sqrt{\sigma_\ell B^2 K_\ell / \mu_\ell}$ from Darcy's law.

References

(1) Carlson, G. A. and Hoffman, M. A. : J. Heat Transfer, Trans. ASME, Series C, Vol.94, No.3 (Aug.1972).

(2) Cosgrove, J. H., Ferrell, J. K. and Carnesale, A. : J. Nucl. Energy, Vol. 21 (1967).

(3) Brinkman, H. C. : Appl. Sci. Res., Vol.A1, p333 (1949).

(4) Marcus, B. D. : NASA CR-2018 (1972).

(5) Winter, E. R. F. and Barsch, W. O. : Advances in Heat Transfer, Vol.7, p219 (1971).

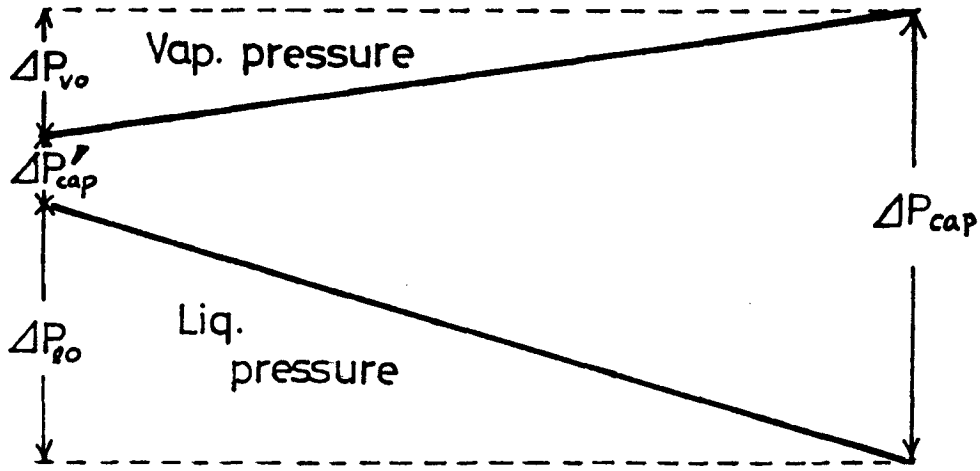

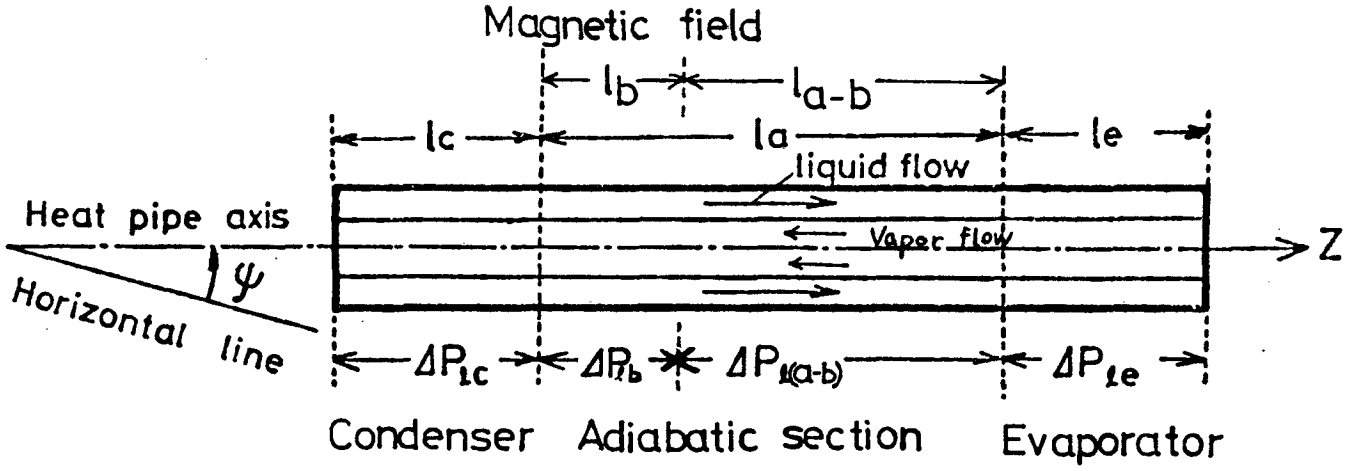

Fig.2-1 Heat pipe schematic diagram

Chapter 3.

Influence of the Magnetic Field on Heat Transport Characteristics of Potassium Heat Pipe

3-1 Introduction

The influence of the magnetic field existing in the adiabatic section on the heat transport characteristics of the potassium heat pipe is experimentally studied. Observations are made about the maximum heat transport rate limited by the maximum wick pumping pressure, about the relation between the heat transport rate and the operating temperature, and about the axial temperature distribution in the absence and in the presence of the magnetic field.

3-2 Experimental Apparatus and Procedure

In the present experiment, potassium is used as the working fluid. The structure of a potassium heat pipe is shown in Fig.3-1. The axial length of the heat pipe is 700 mm and the cross section of the rectangular AISI 304 stainless steel tube is 21x21mm(outer). The wick, made of 200-mesh screen woven by 304 stainless steel wires of 0.053 mm O.D., has the form of a six-layer spiral. The wick thickness is 1.5 mm, that of the wall of the heat pipe 1.0 mm. The axial lengths of the evaporator, the adiabatic and the condenser sections are 200, 300 and 100 mm, respectively. The gas-reservoir having an axial length of 100mm, of the same cross section as the heat pipe, is installed at the

condenser end, for the accumulation of gaseous impurities produced in the heat pipe. The adiabatic section is composed of a double-concentrated rectangular tube for perfect separation of the vapor flow path from the liquid flow. This serves to eliminate the effect of liquid entrainment into the vapor stream, and the wick thickness can be kept constant along the adiabatic section of the heat pipe. The wall thickness of the inner tube is 1.0 mm. Chromel-alumel thermocouples sheathed in stainless steel tubing of 1.0 mm O.D. are arranged on the container wall at positions marked T2~T10, and a similar thermocouple, of 3.2 mm O.D., labeled T1 is inserted into the vapor space at the top end of the evaporator section.

The heat pipe is placed into an electrical furnace and heated by siliconit pyrogen of the double-spiral tube type. The electric power supply to the furnace is controlled for regulation of the furnace temperature and the amount of heat added to the heat pipe is controlled by adjusting the furnace temperature. For heat removal, a copper tube of 8.0 mm O.D. is closely wound around the container wall, with the cooling water flowing through the copper cooling coil.

A DC magnetic field, its strength being adjustable from 0 to 0.6 Tesla, is applied perpendicularly to the adiabatic section of the heat pipe so as to maximize the MHD effect. The axial length of the heat pipe applied by the magnetic field is 7.5 cm.

In the experiment, the furnace temperature T_f is increased in discrete steps, with the mass flow rate of cooling water M_{co}

and the angle of inclination ψ being kept constant, and after each step, the magnetic field is applied to the heat pipe. After application of the magnetic field, the heat transport rate and the temperature in each section are measured under steady condition. With the heat addition to the heat pipe, the heat transport rate increases and finally reaches its maximum. The maximum heat transport rate is measured from the evaporator wick dry-out.

The heat transport rate is evaluated from the mass flow rate and the temperature difference of the cooling water. The temperature signals are directly checked by a digital thermometer and simultaneously recorded by a multi-pen recorder.

3-3 Maximum Heat Transport Rate in the Absence of the Magnetic Field

To know the effect of the magnetic field, the performance characteristics of the heat pipe in the absence of the magnetic field must be made clear. It is assumed that the vapor pressure drop can be neglected in comparison with the liquid pressure drop.

The dependence of the maximum heat transport rate of the potassium heat pipe on the angle of inclination in the absence of the magnetic field is shown in Fig.3-2, where the dotted line is the experimental line fitted to the data. From Eq. (2-21), the heat transport rate is, in the absence of the magnetic field,

$$Q = \lambda(\Delta P_{\ell o} - \rho_{\ell} g l_o \sin\psi)/R_{\ell o} , \qquad (3-1)$$

Then the maximum heat transport rate limited by the maximum wick pumping pressure for liquid is expressed as follows;

$$Q_{max} = \lambda(\Delta P_{\ell o,max} - \rho_\ell g l_o \sin\psi)/R_{\ell o}, \qquad (3\text{-}2)$$

where $\Delta P_{\ell o,max}$ is the maximum wick pumping pressure for liquid. If $\Delta P_{\ell o,max}$ remains constant, Q_{max} depends linearly on $\sin\psi$. In Fig.3-2, the measured value decreases with the increasing angle of inclination and depends linearly on $\sin\psi$ as revealed. Then the heat transport rates are limited by the maximum wick pumping pressure for liquid, but not by the sonic vapor flow or the boiling. In addition, the over-all flow resistance, $R_{\ell o}$, of the wick used in the present experiment can be determined from the gradient of the dependence line in Fig.3-2. The absolute value of the gradient is

$$\lambda \rho_\ell g l_o / R_{\ell o} = 1100 \ (w). \qquad (3\text{-}3)$$

As described in Section 3-6, the axial length of the operating region of the heat pipe is slightly smaller than the heat pipe length under present experimental conditions. Then, by assuming that l_o = 550 mm, $R_{\ell o}$ becomes to be 7.0×10^6 $(s.m)^{-1}$ from Eq.(3-3). The value of $R_{\ell o}$ is used in Section 3-8.

From Eqs.(2-2) and (3-1), the following relation is obtained.

$$\frac{\Delta P_{vo}}{\Delta P_{\ell o}} = \frac{1}{\rho_v}\left(\frac{Q}{\lambda}\cdot\frac{\sqrt{\pi^2-4}}{2A_v}\right)^2\cdot\left(\frac{Q}{\lambda}\cdot R_{\ell o}+\rho_\ell g l_0 \sin\psi\right)^{-1}.$$

This ratio is calculated to confirm the validity of the assumption that the vapor pressure drop can be neglected. Assuming that the vapor is in a saturated condition, the vapor density can be related to the vapor temperature. In Fig.3-3, the heat transport rate is about 100w when the vapor temperature is 500 ^{o}C. Then the ratio of the vapor and the liquid pressure drops is about 3×10^{-3}. When T_v=600 ^{o}C and Q=600 w, the ratio is about 8×10^{-3}. The vapor pressure drop is by two or three orders of magnitude lower than the liquid pressure drop under the present experimental conditions. Hence the vapor pressure drop can be neglected. The heat pipe used in the present experiment has a large area for the vapor flow in comparison with the liquid flow area in the wick. In the case that a heat pipe has a small area for the vapor flow in comparison with the liquid flow area, the vapor pressure drop will not be able to be neglected.

3-4 Heat Transport Characteristics in the Absence of the Magnetic Field

The heat transport characteristics of the heat pipe in the absence of the magnetic field are shown in Fig.3-3 in relation

to the heat transport rate and the vapor temperature in the evaporator section (T1). The solid curve represents the heat transport rate limited by the sonic vapor flow, which is obtained from Levy's equation.[1] The maximum heat transport rate under the present experimental condition of the angle of inclination, ψ =10 deg., is 670 w. In Fig.3-3, the experimental results not only deviate from the sonic limiting curve to the higher temperature, but are also lower than the maximum heat transport rate. In addition, no evaporator wick dry-out was observed under experimental conditions in Fig.3-3. The heat transport rates below Q_{max} are not limited by the sonic vapor flow, the wick pumping and the boiling. In Fig.3-3 it is revealed that the transport rate, Q, depends linearly on the vapor temperature in the evaporator section, T_v, (measured by the thermocouple labeled by T1). The dotted line follows the experimental data, therefore the line represents the heat transport characteristic curve in the absence of the magnetic field, being expressed by

$$Q = \alpha(T_v - T_o), \qquad (3\text{-}4)$$

where α and T_o are constant under this experimental condition. In Fig.3-3, these are 4.6 w/deg. and 470 ^{o}C, respectively. In the present chapter, the heat transport characteristics shown in relation to the heat transport rate, Q, and the operating temperature, T, are called "Q-T characteristics" and the dependence line in the Q-T figure, i.e. Eq.(3-4), is also called the "Q-T line".

The Q-T characteristics of the potassium heat pipe under

the various angles of inclination are shown in Fig.3-4. As seen in Fig.3-4, the Q-T line shifts to a higher vapor temperature range with a constant gradient, with increasing angle of inclination. Then it is evident that not only the maximum but also the heat transport rate corresponding to the same vapor temperature decreases with the angle of inclination.

3-5 Heat Transport Characteristics in the Presence of the Magnetic Field

The Q-T characteristics of the heat pipe in the presence of the magnetic field are shown in Fig.3-5(a)~(c) under various furnace temperatures but constant ψ which is 10 deg.. Each plot in these figures represents an average of ten measurements, and the bars indicate the extent of scatter in the measured values. In these figures, the heat transport rate decreases, but the vapor temperature increases, with increasing field strength under each constant furnace temperature. In addition, when the furnace temperature is low (T_f = 600 ^{o}C), the influence of the magnetic field on Q and T_v is very small in comparison with higher furnace temperatures (T_f = 700, 750 ^{o}C). Under a constant field strength, a decrease of the heat transport rate and an increase of the vapor temperature become prominent with the increasing furnace temperature.

For a further discussion of the Q-T characteristics in the magnetic field, the δ-value is introduced and defined as follows;

$$\delta \equiv Q/(T_v - T_o) , \qquad (3\text{-}5)$$

where T_o is 470 ^oC for ψ = 10 deg..

If the δ-value is constant at any operating condition, it can be said that the heat transport rate depends linearly on the vapor temperature and then the δ-value is equal to the gradient α of the Q-T line. The δ-values with the various field strengths and the various furnace temperatures are shown in Table 3-1, where these are obtained from Eq.(3-5), using the data in Fig.3-5(a)~(c) for Q and T_v. As seen from Table 3-1, the δ-value is constant with a constant field strength, in spite of the different furnace temperatures, but it decreases with increasing field strength. Thus the heat transport rate in the magnetic field also depends linearly on the vapor temperature. Furthermore the gradient of the Q-T line, α, decreases with the intensification of the magnetic field strength.

3-6 Influence of the Magnetic Field on Axial Temperature Distribution

The typical axial temperature distribution in the absence, or in the presence, of the magnetic field is shown in Fig.3-6. As revealed in this figure, the temperature decreases toward the condenser section and the temperature gradient rises steeply at the end of the adiabatic section. In addition, the wall temperature T10 at the condenser end is equal to the room temperature. Since temperature T10 is below the freezing point of potassium, the working fluid in the portion of the condenser section is solid. Then the axial length of the

operating region of the heat pipe is slightly smaller than the whole heat pipe length. From the axial temperature distribution it is presumed that the gaseous impurities may accumulate at the condenser end and impede the vapor flow, resulting in the decrease of the effective area of vapor condensation.

After applying the magnetic field, the wall temperatures T6~T8 in the adiabatic section increase, and so does vapor temperature T1, but the wall temperature T9 at the end of the adiabatic section decreases by several degrees. The results show that the magnetic field has an effect on the axial temperature distribution as well as on the Q-T characteristics.

3-7 Maximum Heat Transport Rate in the Presence of the Magnetic Field

The magnetic field was applied on the heat pipe which steadily transported the heat. The heat transport rate was near the maximum heat transport rate. The steady state of axial temperature distributions before and after application of the magnetic field are shown in Fig.3-7. Before the application, the vapor temperature in the evaporator section is about 600 ^{o}C. After the application, the vapor temperature is about 800 ^{o}C which is equal to the furnace temperature. It is clear that the evaporator wick is dried out, but the dry-out is partial since the wall temperature T3, T4 and T5 do not change. With the increase of the magnetic field strength, the pressure drop of liquid in the wick increases due to the MHD effect, the maximum heat transport rate decreasing with it. The dry-out is caused by an excessive addition of heat to the heat pipe over the maximum heat transport rate. The

experimental results show that the magnetic field impedes the liquid flow in the wick and so reduces the maximum heat transport rate. After the dry-out, the amount of heat added to the heat pipe decreases with the temperature rising in the dry-out region.

3-8 Discussion

(1) Q-T characteristics in the absence of the magnetic field

The following discussion is made on the influence of the gravitational force on the Q-T characteristics. The heat transport rate is expressed by Eq.(3-1), whereas the Q-T line is expressed by Eq.(3-4). Using ψ_i for ψ in Eq.(3-1), the following equation is obtained from Eqs.(3-1) and (3-4).

$$\lambda(\Delta P_{\ell o} - \rho_\ell g l_o \sin\psi_i)/R_{\ell o} = \alpha(T_v - T_o) \ . \qquad (3\text{-}6)$$

Equation (3-6) represents the relation of the wick pumping pressure $\Delta P_{\ell o}$ for the liquid to the vapor temperature T_v at the given angle of inclination, ψ_i. At $\psi = \psi_{i+1}$, the heat transport rate is

$$Q(\psi_{i+1}) = \lambda(\Delta P_{\ell o} - \rho_\ell g l_o \sin\psi_{i+1})/R_{\ell o} \ . \qquad (3\text{-}7)$$

Assuming that $\Delta P_{\ell o}$ is a function of T_v alone, the following equation is obtained from Eqs.(3-6) and (3-7).

$$Q(\psi_{i+1}) = \alpha(T_v - T_o) + \lambda\rho_\ell g l_o(\sin\psi_i - \sin\psi_{i+1})/R_{\ell o} \ . \qquad (3\text{-}8)$$

The equation (3-8) represents the Q-T line at $\psi=\psi_{i+1}$. With increasing angle of inclination ($\psi_i \rightarrow \psi_{i+1}$), the Q-T line shifts to a higher temperature range with a constant gradient. This tendency is similar to the experimental results shown in Fig.3-4. As for the same vapor temperature, the following relation is obtained from Eq.(3-8).

$$\frac{Q(\psi_1) - Q(\psi_2)}{Q(\psi_1) - Q(\psi_3)} = \frac{\sin\psi_2 - \sin\psi_1}{\sin\psi_3 - \sin\psi_1} . \qquad (3\text{-}9)$$

In Fig.3-4, the difference of the heat transport rate corresponding to the same vapor temperature at any Q-T point between the cases of ψ_1=5 and ψ_2=10 deg. is 95 W, and the difference between the cases of ψ_1=5 and ψ_3=15 deg. is 190 W. Then the ratio between these values is 0.50, while the value obtained from the right-hand side of Eq.(3-9) is 0.50. From the agreement between these values it is found that the decrease of the heat transport rate corresponding to the same vapor temperature is caused by the reduction of the wick pumping ability resulting from the gravitational force without a change of $\Delta P_{\ell o}$. Then, it can be concluded that the wick pumping pressure $\Delta P_{\ell o}$ is a function of the vapor temperature T_v alone and is not influenced by the gravitational force acting on the liquid flow in the wick.

(2) Q-T characteristics in the presence of the magnetic field

Subsequently, the discussion is made on the influence of the magnetic force on the Q-T characteristics. From Eq.(2-21), the

heat transport rate in the presence of the magnetic field is

$$Q = \lambda(\Delta P_{\ell o} - \rho_\ell g l_o \sin\psi)/(1+\zeta)R_{\ell o} \ . \qquad (3\text{-}10)$$

In the absence of the magnetic field, the following relation is obtained from Eqs.(3-1) and (3-4) using $\alpha(0)$ for α.

$$\lambda(\Delta P_{\ell o} - \rho_\ell g l_o \sin\psi)/R_{\ell o} = \alpha(0)\ (T_v - T_o) \ , \qquad (3\text{-}11)$$

where $\alpha(0)$ represents the gradient of the Q-T line in the absence of the magnetic field. Since the wick pumping pressure, $\Delta P_{\ell o}$, is a function of only the vapor temperature, Tv, the following equation is obtained from Eqs.(3-10) and (3-11).

$$Q = \alpha(B)(T_v - T_o) \ , \qquad (3\text{-}12)$$

$$\text{where } \alpha(B) \equiv \alpha(0)/(1+\zeta) \ . \qquad (3\text{-}13)$$

The equation (3-12) represents the Q-T line and $\alpha(B)$ is the gradient of the line in the presence of the magnetic field. Since the MHD effect on the flow can be regarded as an increase of the flow resistance, the gradient of the Q-T line decreases with the increasing field strength as shown in Table 3-1.

(3) Decrease of the heat transport rate

The following discussion is made about the influence of the magnetic field on the heat transport rate of the heat pipe. For the discussion, the decreasing rate of the heat transport rate, being represented by η, is introduced and defined as

follows;

$$\eta = 1 - Q(B)/Q(0), \qquad (3\text{-}14)$$

where Q(0) and Q(B) are the heat transport rates in the absence and in the presence of the magnetic field, respectively(other conditions being the same). Using Q(B) for Q and $\alpha(B)$ for α in Eq.(3-4), the decreasing rate of the heat transport rate corresponding to the same vapor temperature T_v is obtained from Eqs.(3-4) and (3-14) as follows ;

$$\eta_{T_v} = 1 - \alpha(B)/\alpha(0) , \qquad (3\text{-}15)$$

The dependence of η_{T_v} on the magnetic field strength is shown in Fig.3-8, where the solid circles are obtained from Eq.(3-15) using the δ-values shown in Table 3-1 for $\alpha(B)$. The blanked circles represent the decreasing rate η_{T_f} of the heat transport rate for constant furnace temperatures.

It is mentioned that the decrease of the heat transport rate in the magnetic field depends on the heating condition to the heat pipe. When the magnetic field is applied to the heat pipe under a constant furnace temperature, the vapor temperature increases by a few degrees as shown in Fig.3-5(a)~(c). Since the increase of the vapor temperature corresponds to the increase of the wick pumping pressure, as seen in Eq.(3-11), the influence of the magnetic field on the heat transport rate is reduced. Then the blanked data (η_{T_f}) in Fig.3-8 are slightly smaller than the solid ones (η_{T_v}). The solid curve in Fig.3-8 is obtained from the calculation described in the next section.

(4) The permeability of the wick in the magnetic field

The experimental results of η_{T_V} shown in Fig. 3-8 can be used for the discussion on the MHD effect in the wick.

From Eqs.(3-13) and (3-15), the following equation is obtained.

$$\eta_{T_V} = \zeta/(1+\zeta) \quad . \tag{3-16}$$

To discuss the MHD effect in the wick, ζ is estimated in the following. Usually, the wick is surrounded by a container wall, which is made of electrically conducting material such as stainless steel. In this case, the coefficient β might be large due to the presence of the conducting wall and then the increase of frictional pressure loss due to the change of permeability could be neglected in comparison with the magnetic pressure loss. On the assumption that the influence of the magnetic field on permeability can be neglected, ζ is expressed as follows ;

$$\zeta = \frac{l_b}{l_a + \frac{1}{2}(l_e+l_c)} \frac{\beta \sigma_\ell B^2 K_\ell}{\mu_\ell} . \tag{3-17}$$

The permeability, K_ℓ, can be obtained from Eq.(2-18) by estimating A_{eff}. Then, to estimate the dependence of ζ on the magnetic field strength, the following discussion is made on A_{eff} and β. The cross section of the heat pipe is shown in Fig. 3-9 , and the analytical model for the wick structure is schematically shown in Fig.3-10. The wick structure is composed of the multi-layer mesh screen, of 2d thickness and the walls

of b_w thickness surrounding the wick. The wick has the thickness of b_m and the width of a, and d is the diameter of mesh wires. The mesh screens are arranged parallel to the walls. The liquid flows through the slits between the screens in the axial direction of the heat pipe. The axial flow within the mesh screen is neglected since the mesh wires act as submerged obstacles against the axial flow in the screen. Then the effective flow cross section, A_{eff}, for liquid is expressed as follows ;

$$A_{eff} = 4a(b_m - 2nd) , \qquad (3-18)$$

where n is the number of mesh screen layers in the wick.

In a flow between electrically conducting parallel plates, β is expressed as follows ;[2]

$$\beta = C/(1+C) , \qquad (3-19)$$

where C is the ratio of the electrical resistance of fluid to the wall. Equation (3-19) is often used for the estimation of β in various flow channel structures, such as a rectangular pipe and a circular pipe.[2] In the present chapter, equation (3-19) is also used for the estimation of β in the wick. From Eq.(3-19), the estimation of β can be attributed to that of C. The heat pipe wick has the mesh screens in it. The electrical conductance of the screens can be neglected in comparison with the conductance of the outer and the inner walls,

since the screen thickness is much thinner than the wall. Then C is expressed as follows ;

$$C = (\sigma_w b_w/\sigma_\ell)/(A_{eff}/8a) \ , \qquad (3\text{-}20)$$

where σ_w and σ_ℓ are the electrical conductivities of the wall and the liquid, respectively. From Eqs.(3-18), (3-19) and (3-20), the following equation is obtained ;

$$\beta = \{1 + \sigma_\ell (b_m - 2nd)/(2\sigma_w b_w)\}^{-1} \ . \qquad (3\text{-}21)$$

In the present experiment, b_m, b_w and d are 1.5, 1.0 and 0.053mm respectively, and 4a is 70 mm. Then A_{eff} becomes 6.0×10^{-5} m^2 from Eq.(3-18) and β becomes 0.53 from Eq.(3-21). The overall flow resistance, $R_{\ell o}$, is 7.0×10^{6} $(s.m)^{-1}$, which is obtained in Section 3-3 from the experiment of the potassium heat pipe in the absence of the magnetic field. Using these values, K_ℓ is obtained from Eq.(2-18) and is 2.4×10^{-10} m^2. The dependence of ζ on the magnetic field strength can be calculated by Eq.(3-17) using these values of β and K_ℓ obtained from the above discussion. The dependence of η_{T_v} on B is shown in Fig. 3-8, where the solid curve is obtained from a calculation using Eq.(3-17) for ζ. Equation (3-17) is based on the assumption that the influence of the magnetic field on the permeability can be neglected. As shown in this figure, the experimental results can be well described by the predicted curve. Then it is said that the influence of the magnetic field

on the permeability can be neglected. Coefficient β is increased by the presence of the electrically conducting wall and then the magnetic pressure loss becomes too large in comparison with the increase of the frictional pressure loss due to the change of permeability. As the result, the influence of the magnetic field on the permeability can be neglected. With a non-conducting container wall, the permeability might be influenced by the magnetic field. However, practically speaking, the container wall of the heat pipe is made of electrically conducting material such as stainless steel and then the coefficient β increases. Any discussion of the subject of non-conducting walls would be beyond the scope of this thesis.

3-9 Concluding Remarks

Summarizing the discussions in this chapter, the following conclusions can be drawn from the present experiment.

(1) The wick pumping pressure is a function of only the vapor temperature.

(2) The heat pipe conductance suffers from the MHD effect on the liquid flow in the wick.

(3) In the heat pipe wick, the influence of the magnetic field on the permeability in Darcy's law can be neglected.

So far, the effect of the magnetic field on the performance characteristics of heat pipes was discussed only from the view point of the decrease of the maximum heat transport rate, but the present experimental results show that the heat pipe conductance under any operating condition of the heat transport

rate depends on the magnetic field. Then it is clear that the control of the conductance of liquid metal heat pipe is possible by the liquid flow control by using the magnetic field.
On the other hand, in the heat pipe application to the CTR blanket, the change of the heat pipe conductance becomes serious since the magnetic field for plasma confinement is very strong.

In addition, it is presumed from the axial temperature distribution in the present experiment that a small amount of non-condensable gas might be present in the heat pipe. Then the heat transport characteristics would be influenced by the gas. The influence of the gas on the characteristics is discussed in Chapter 6.

References

(1) Levy, E. K. : J. Eng. for Industry, Trans. ASME (Nov. 1968).

(2) Hoffman, M. A. and Carlson, G. A. : UCRL-51010.

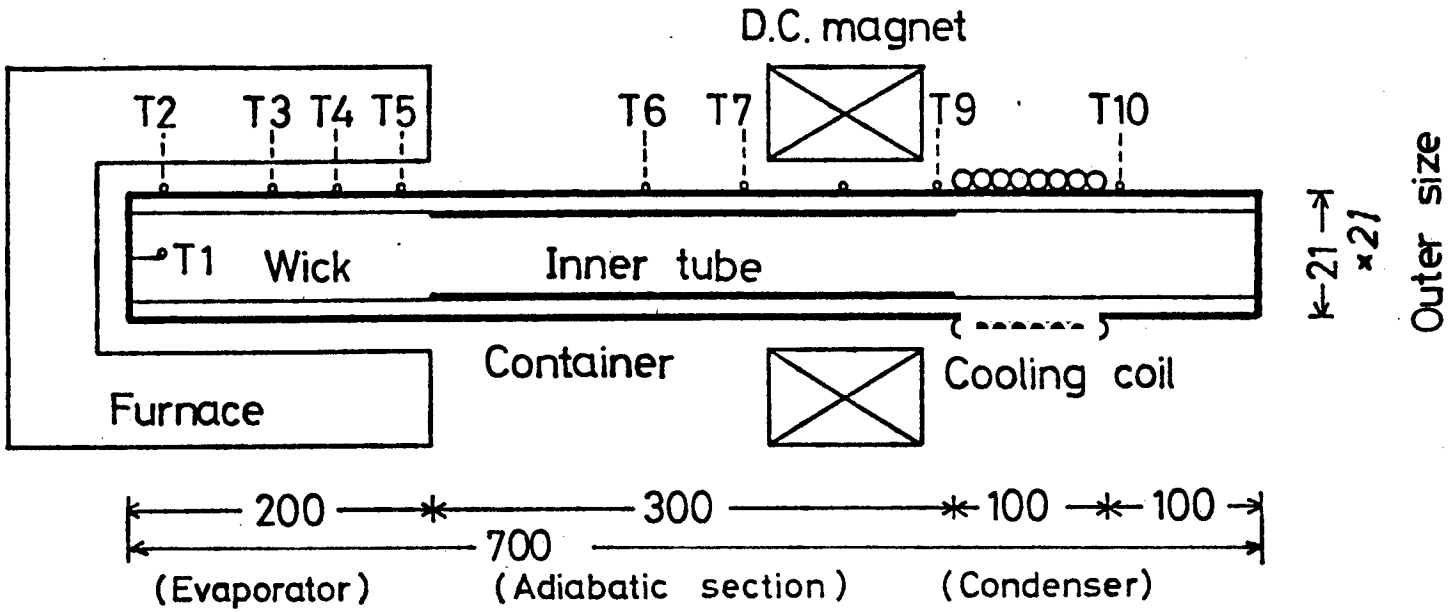

Fig.3-1 Schematic diagram of potassium heat pipe and experimental apparatus

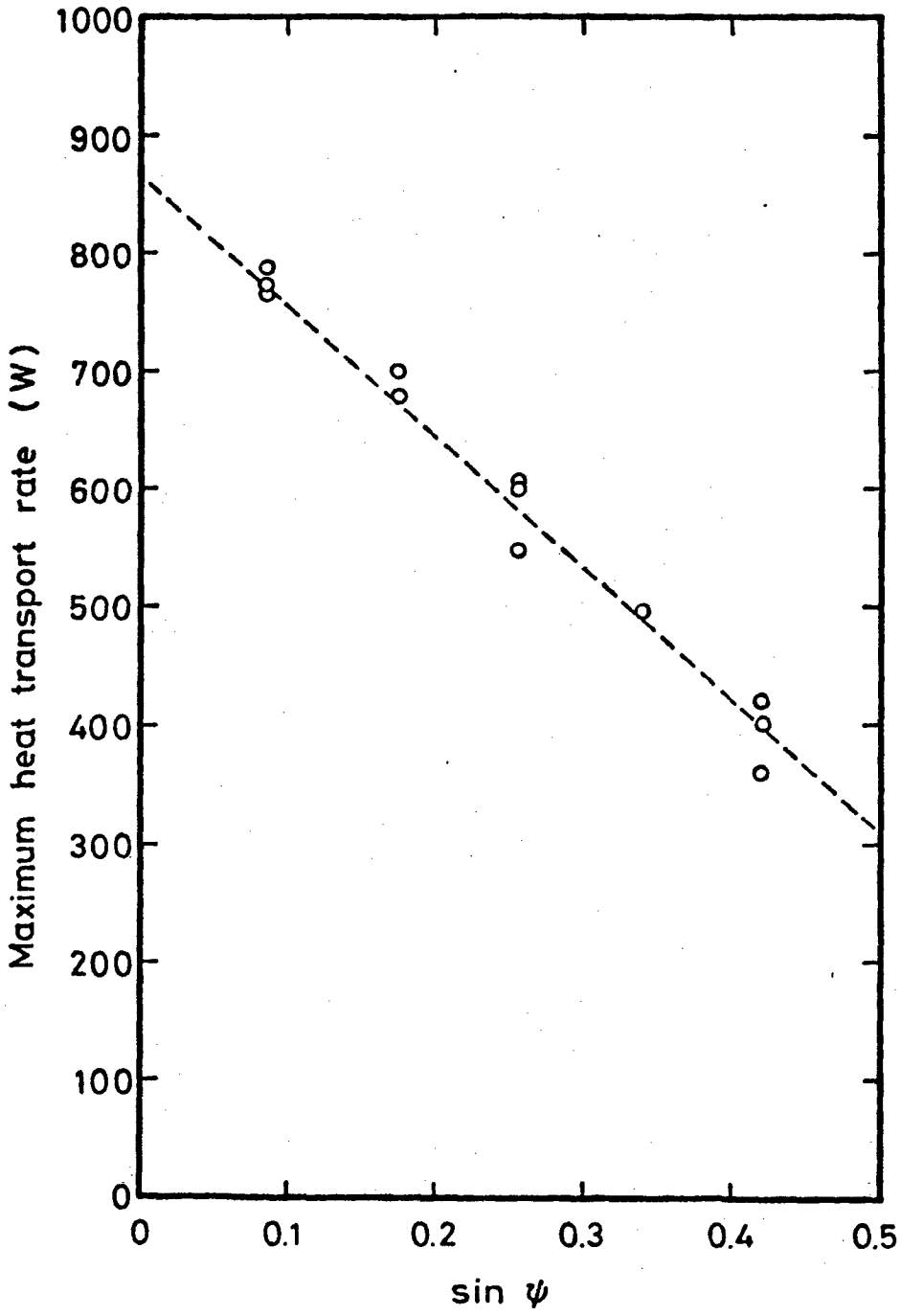

Fig.3-2 Dependence of Q_{max} on sin ψ

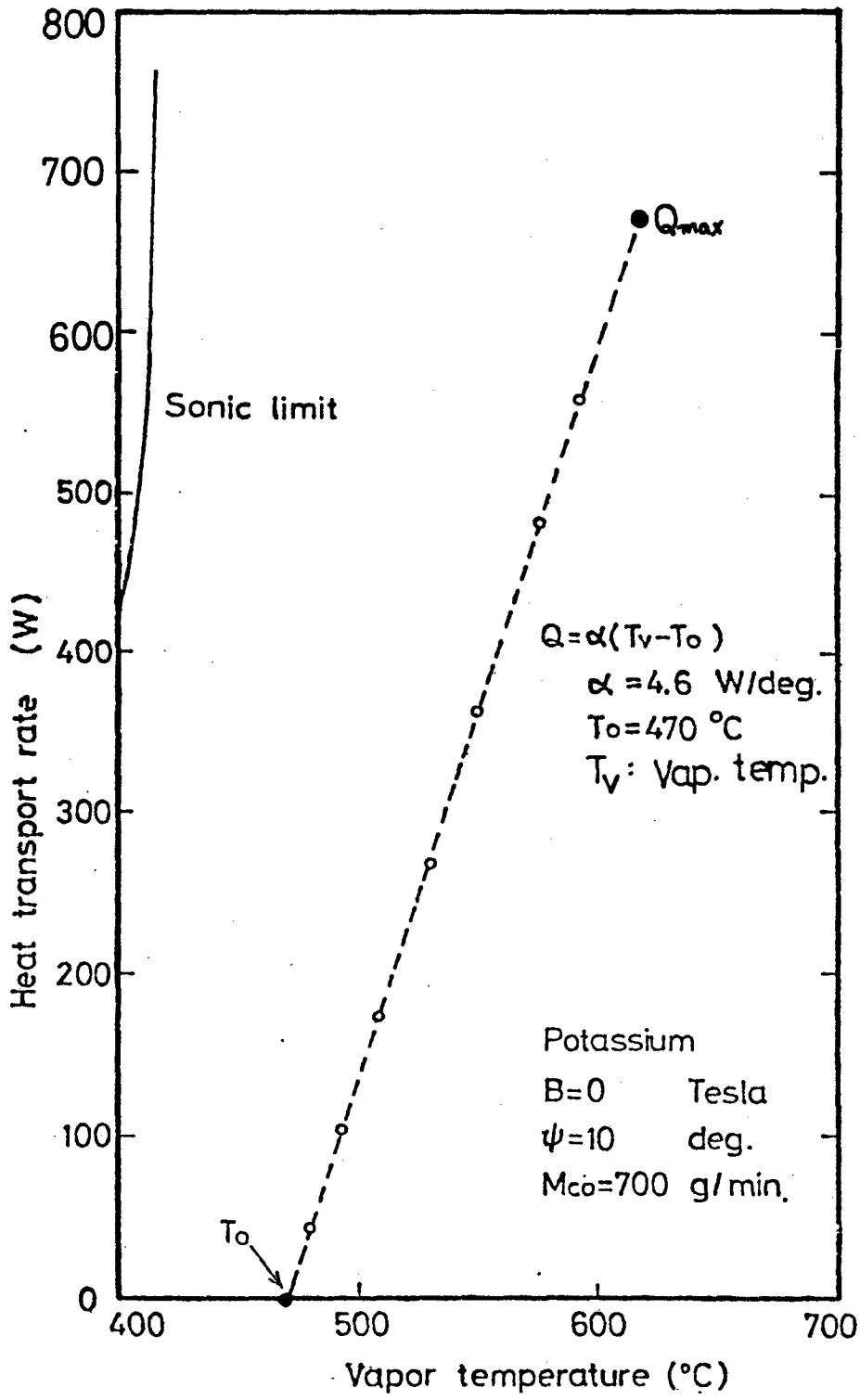

Fig.3-3 Q-T characteristics in the absence of the magnetic field

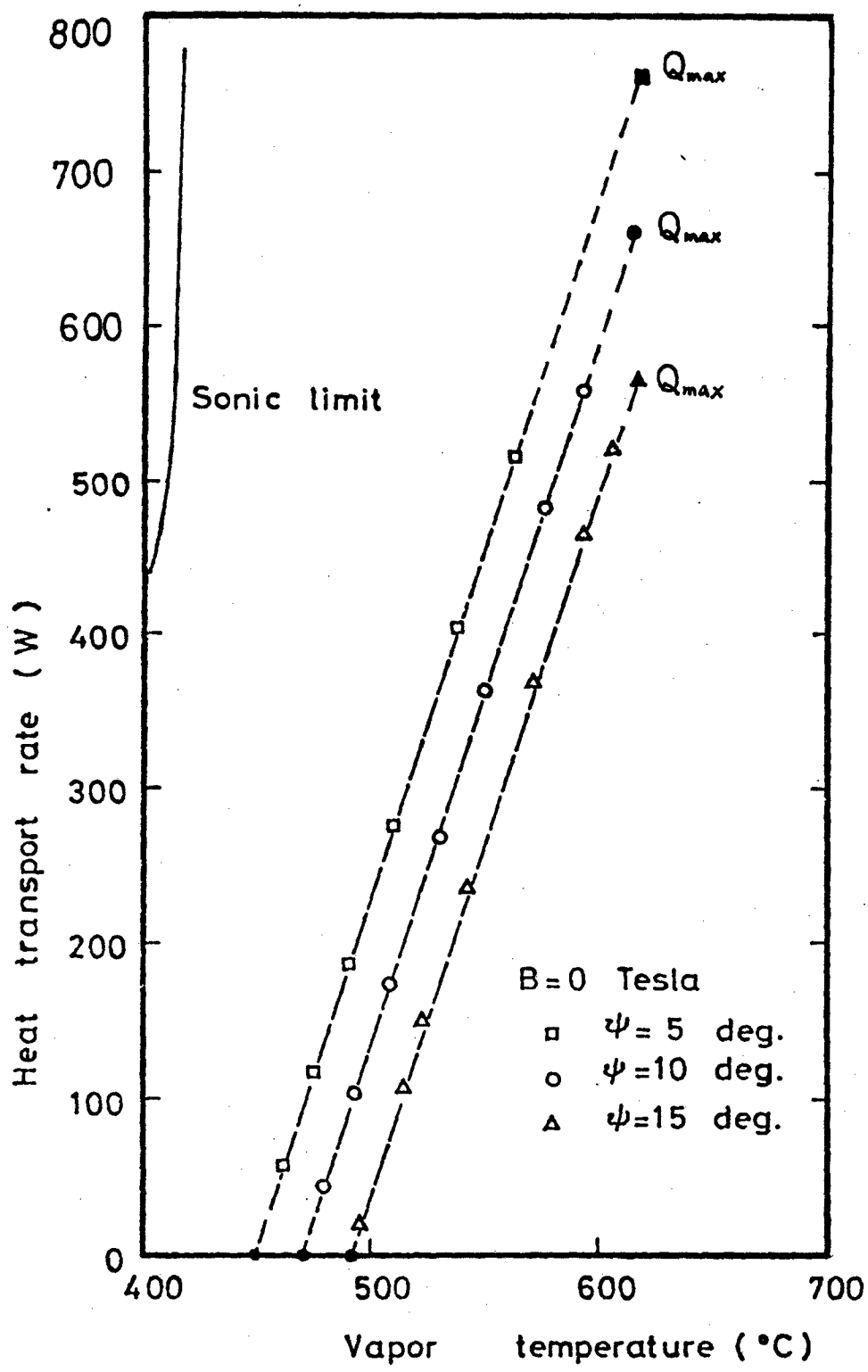

Fig.3-4 Influence of the gravity on Q-T characteristics

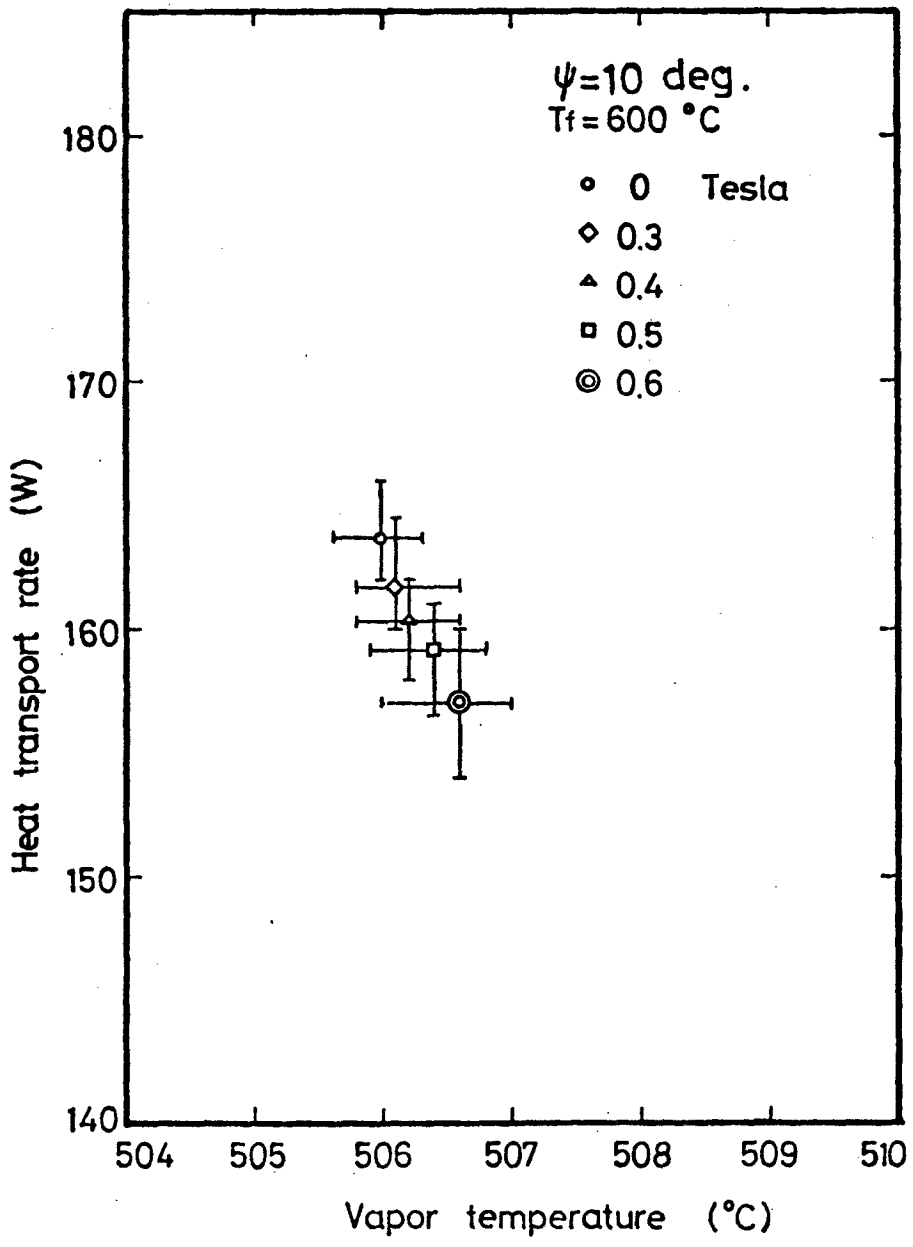

Fig.3-5(a) Q-T characteristics in the presence of the magnetic field under a constant furnace temperature (T_f=600 °C)

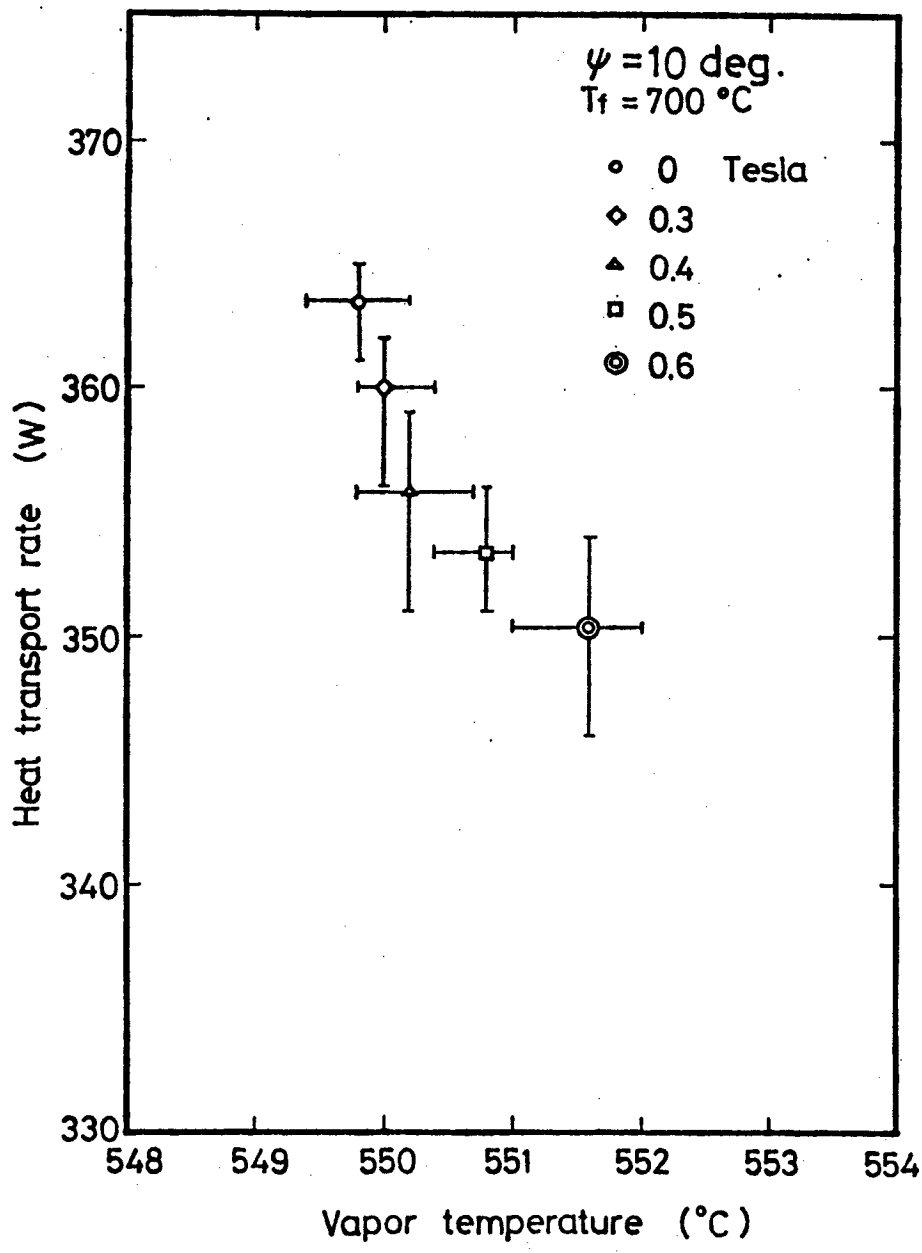

Fig.3-5(b) Q-T characteristics in the presence of the magnetic field under a constant furnace temperature (T_f=700 ^{o}C)

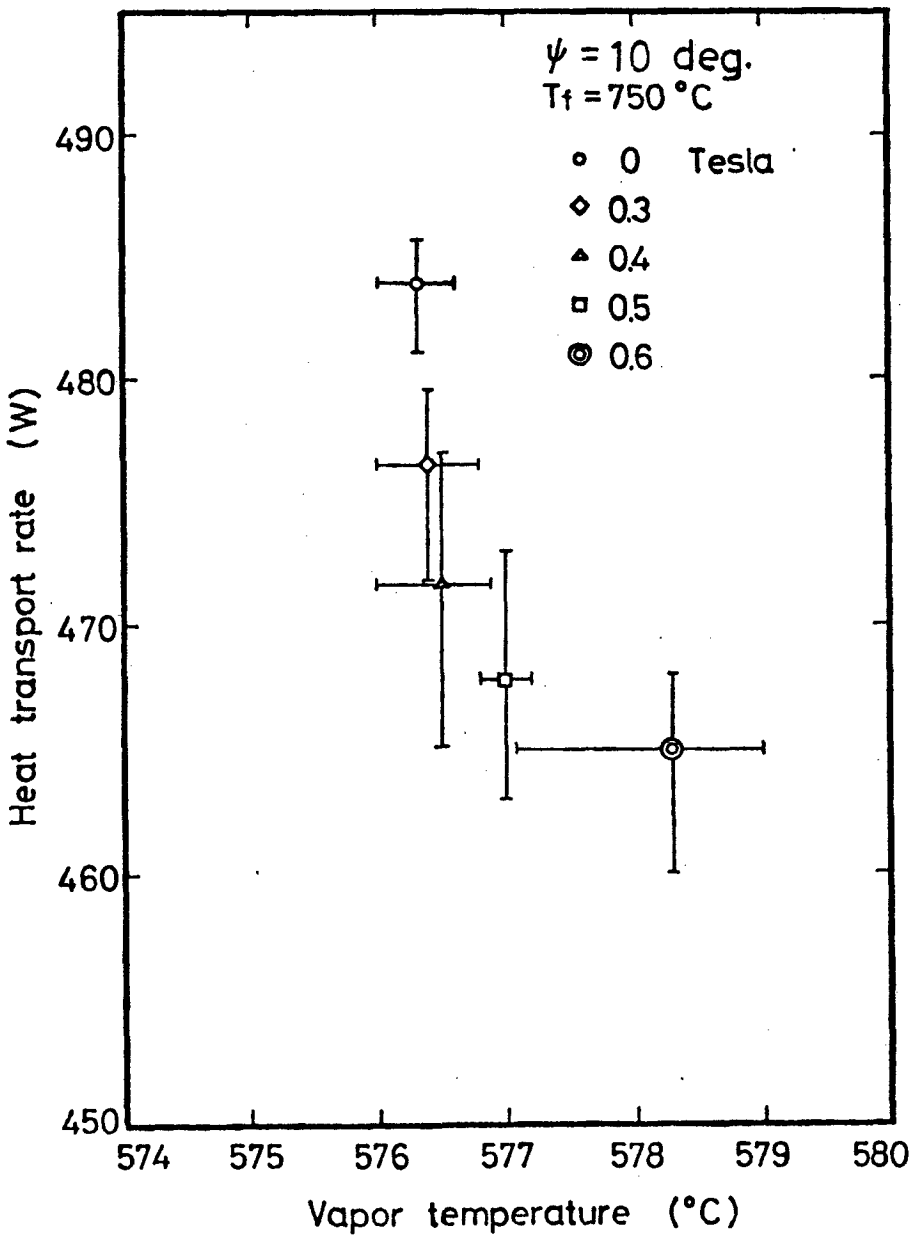

Fig.3-5(c) Q-T characteristics in the presence of the magnetic field under a constant furnace temperature (T_f=750 °C)

Table 3-1 δ-values

B(Tesla)	T_f (^oC)		
	600	700	750
0	4.6	4.6	4.6
0.3	4.5	4.5	4.5
0.4	4.4	4.4	4.4
0.5	4.4	4.4	4.4
0.6	4.3	4.3	4.3

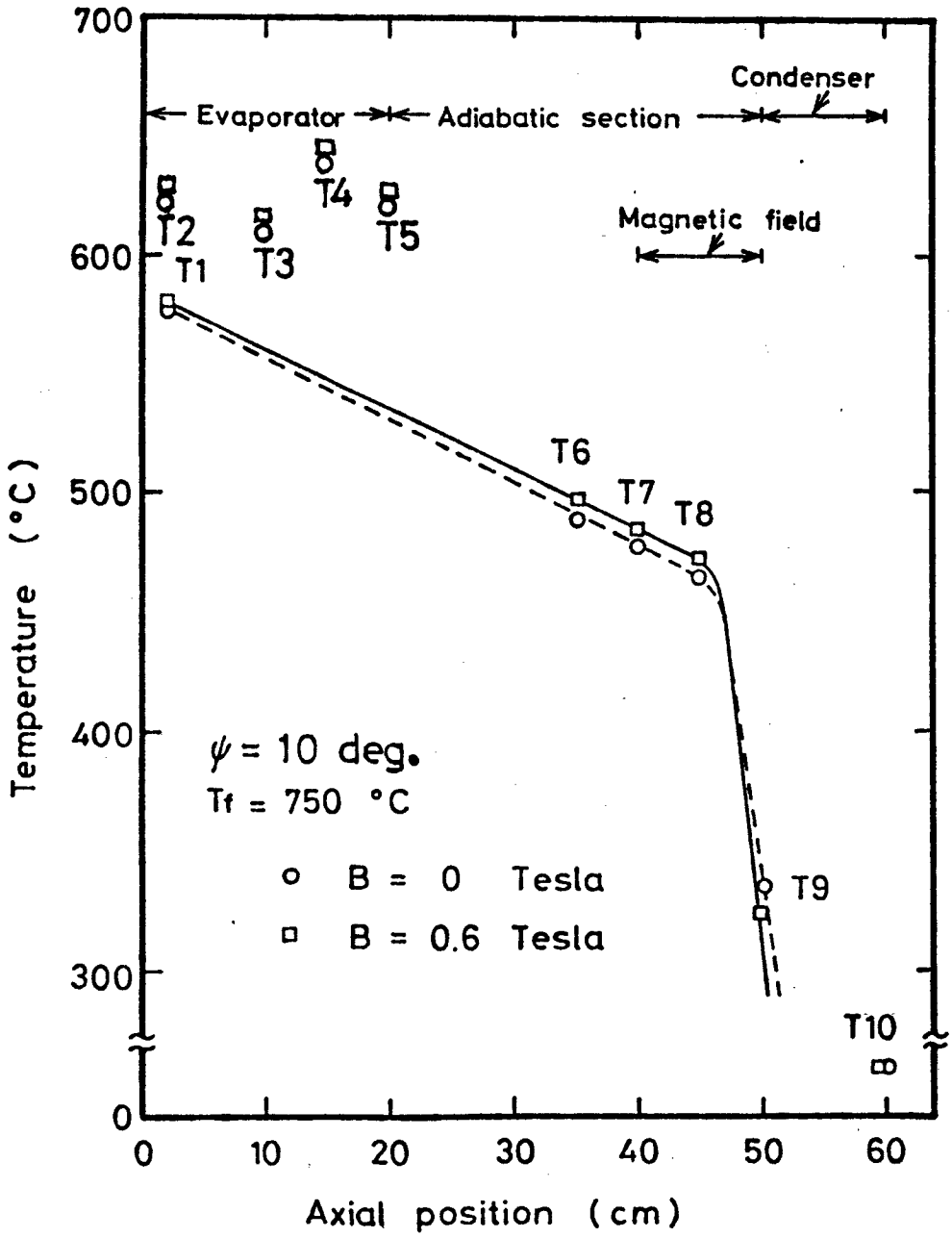

Fig.3-6 Influence of the magnetic field on axial temperature distribution

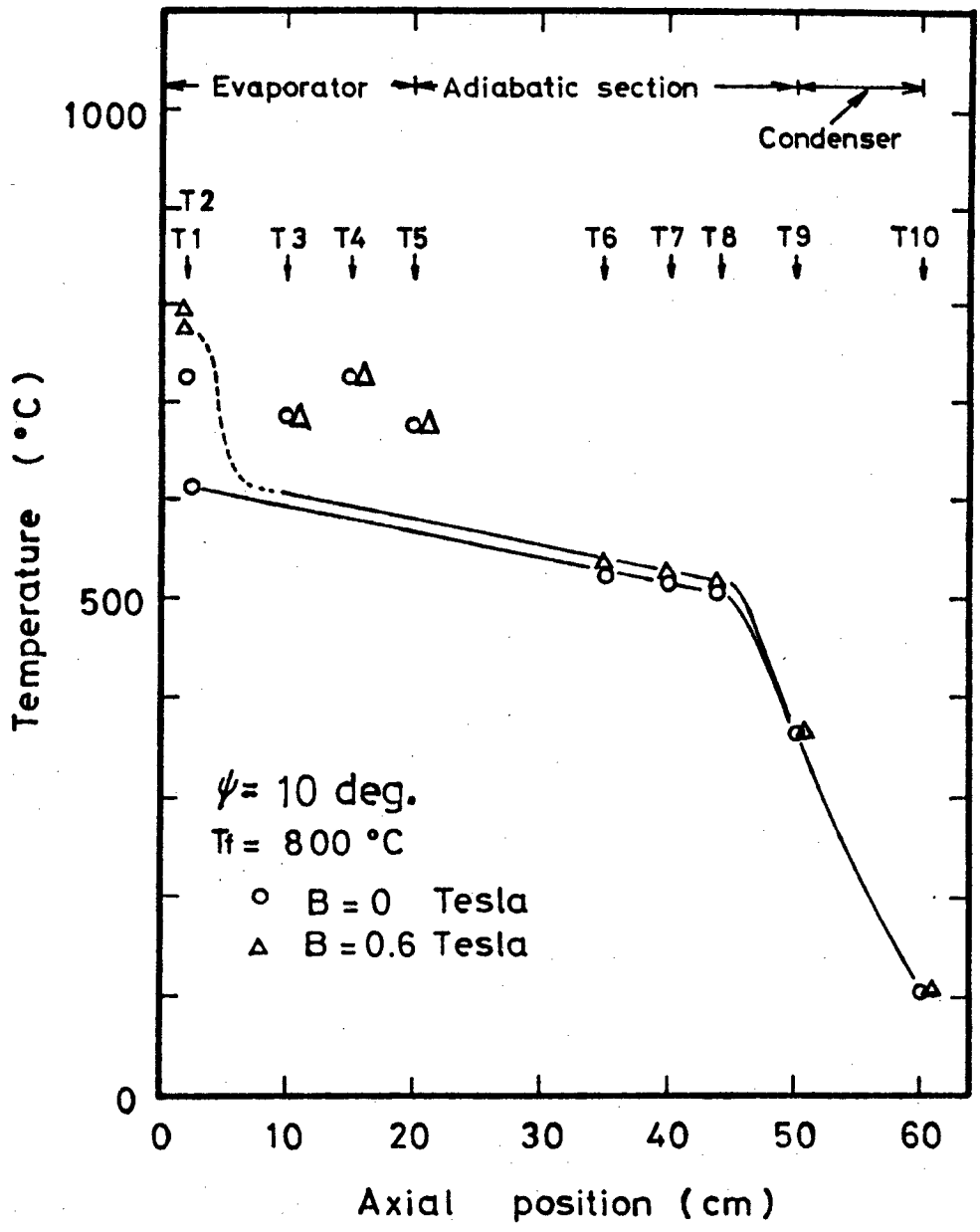

Fig.3-7 Axial temperature distribution after the evaporator wick dry-out

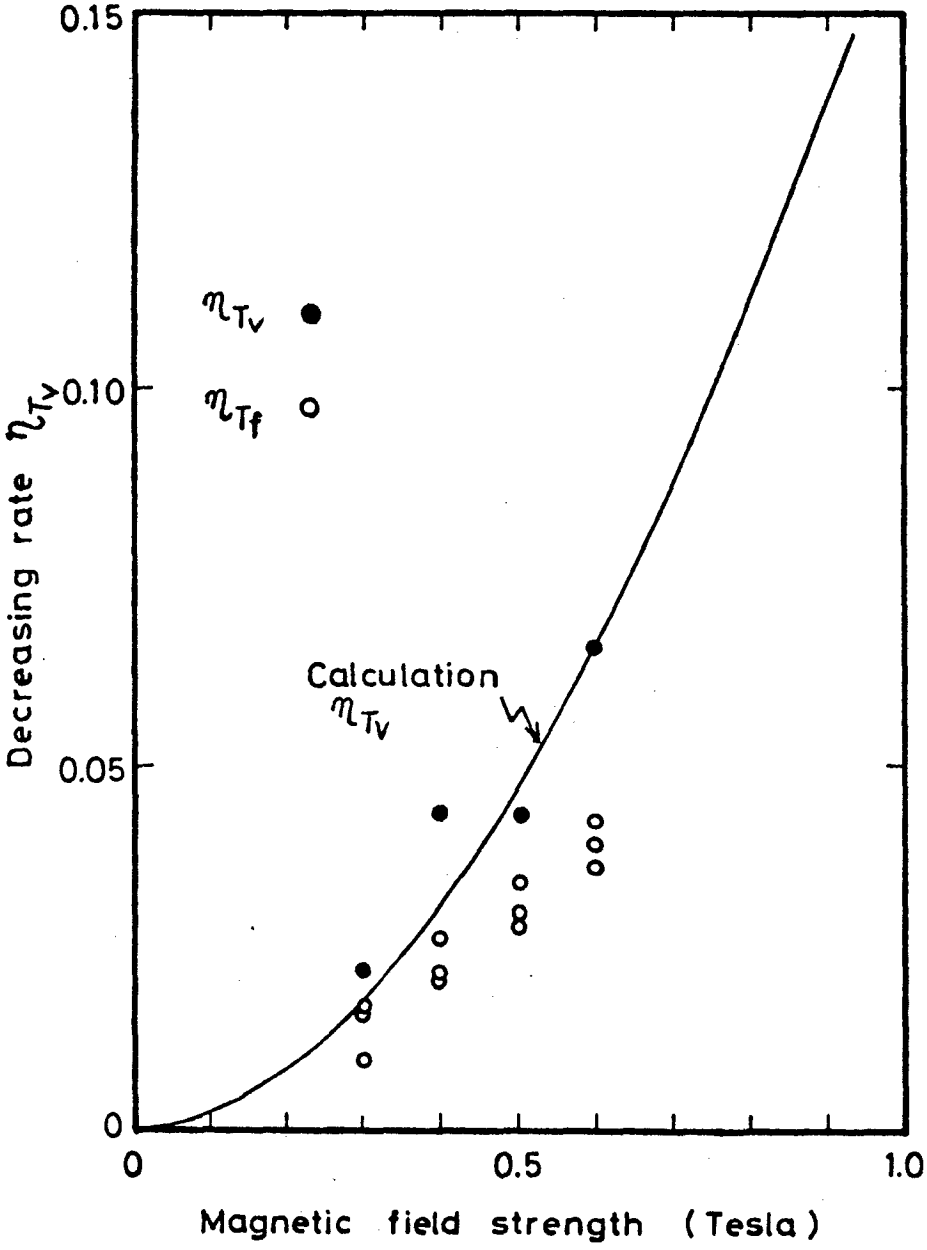

Fig.3-8 The dependence of η_{Tv} on the magnetic field strength

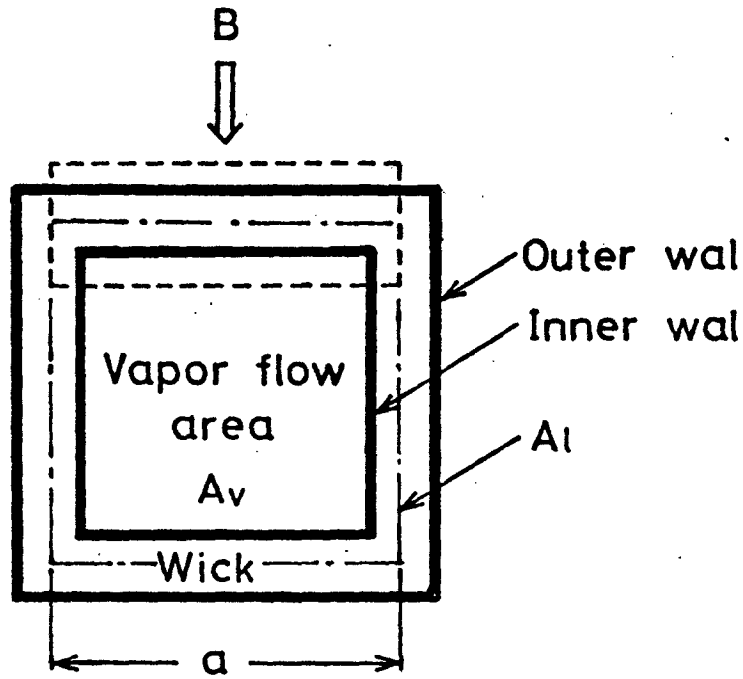

Fig.3-9 Cross section of the heat pipe

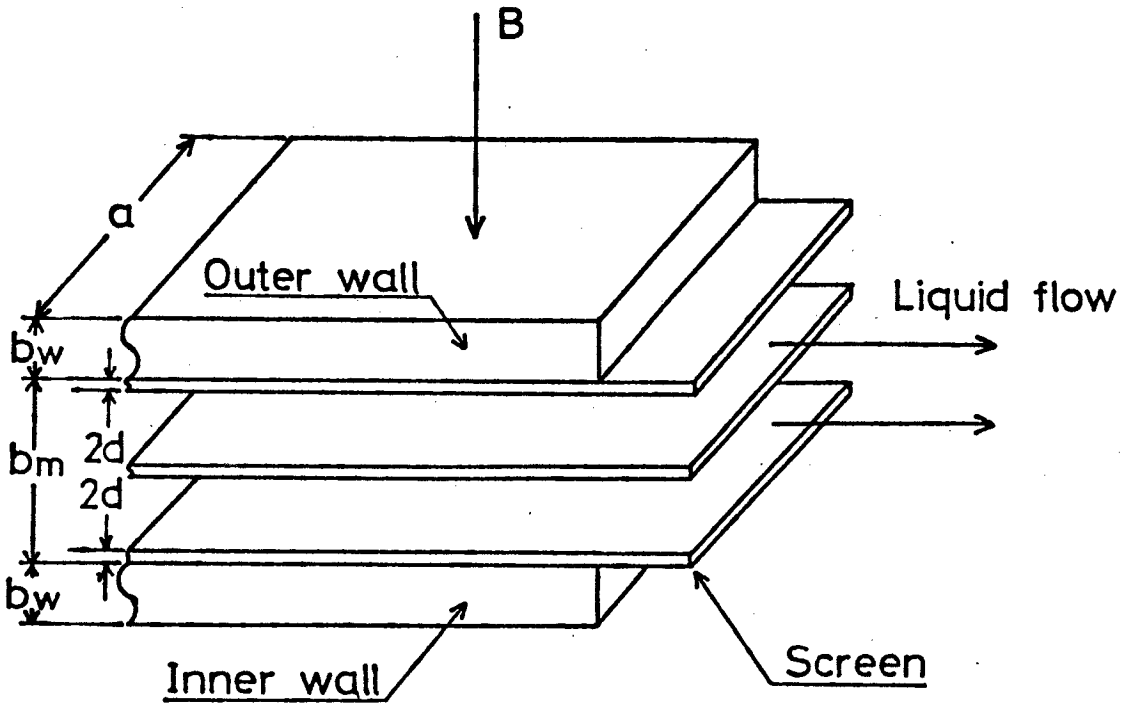

Fig.3-10 Analytical model for wick structure

Chapter 4

Wick Pumping Limit in the Magnetic Field

4-1 Introduction

The wick structure of multi-layer mesh screen is the most popular structure of porous wicks. In the case of tightly wrapped or sintered screen wicks, a porosity in the wick is equal to the porosity of the mesh screen itself. In this case, the relation between the permeability and the wick porosity is expressed as follows ;[1]

$$K_\ell = \frac{1}{122}\frac{d^2\varepsilon^3}{(1-\varepsilon)^2}, \qquad (4\text{-}1)$$

where d is the screen wire diameter and ε is the wick porosity.

With regard to loosely wrapped screen wicks, the permeability depends on the gaps between adjacent layers. The loosely wrapped screen wick has a smaller flow resistance than the tightly wrapped wick. Thus, preference must be given to loosely wrapped rather than tightly wrapped screens.

When dealing with the wick pumping limit, the permeability of the wick should be known. However, the relation between the permeability and the wick porosity is not known in the case of the loosely wrapped screen wick. In this chapter, the permeability of the loosely wrapped screen wick is estimated and the wick pumping limit in the magnetic field is discussed.

4-2 Estimation of Permeability

In this section, the dependence of the permeability on the porosity of the wick is estimated by using the hydraulic radius of the wick. According to Fig.3-10 the porosity ε is expressed as follows;

$$\varepsilon = 1 - 2nd(1-\varepsilon_m)/b_m \ , \tag{4-2}$$

where ε_m is the porosity of the mesh screen itself.
The details of the mesh screen are shown in Fig. 4-1.
The screen is woven by wires of a diameter d.

Under the zero magnetic field, the mean axial velocity of liquid in the wick is expressed by using a hydraulic radius r_h as follows ;[2]

$$v_\ell = r_h^2(\Delta P_\ell - \rho_\ell g l \sin\psi)/(2\mu_\ell l) \ , \tag{4-3}$$

where ΔP_ℓ is the pressure difference at distance l.
Approximating dP_ℓ/dz in Eq.(2-4) with $-\Delta P_\ell/\Delta z$, and using l for Δz, the following relation is obtained from Eqs.(2-4) and (4-3).

$$K_\ell = r_h^2/2 \ . \tag{4-4}$$

From the definition of the hydraulic radius, r_h is expressed as follows ;[2]

$$r_h = V/S \ , \tag{4-5}$$

where S is the total wetted surface in the wick and V is the volume available for flow. Within the unit cell shown in Fig.4-1, the wetted surface and the volume available for flow, being represented with S_u and V_u respectively, are approximately expressed as follows ;

$$\begin{cases} S_u = 2\pi d(2d+f) \\ V_u = 2d(d+f)^2 - 2\pi(d/2)^2(2d+f) \ . \end{cases} \tag{4-6}$$

Using S_u and V_u, S and V are

$$\begin{cases} S = alnS_u/(d+f)^2 + 2al \\ V = alnV_u/(d+f)^2 + al(b_m-2nd) \ . \end{cases} \tag{4-7}$$

From Eqs.(4-4)~(4-7), the following equation is obtained.

$$K_\ell = \frac{1}{32}\left\{\frac{(2b_m+d)(d+f)^2}{\pi nd(2d+f)+(d+f)^2} - d\right\}^2 \ . \tag{4-8}$$

In Eq.(4-8), K_ℓ is obtained on the assumption that the liquid flow path through the wick has a length l, which is the same as the wick length. Actually, the liquid flows in a very tortuous path and then the length of the liquid flow path is larger than the wick length. Therefore, equation (4-8) gives too large a value K_ℓ for a given pressure gradient, hence the right-hand side of Eq.(4-8) should be diminished by using an accommodation factor ϕ.

$$K_\ell = \frac{1}{32\phi}\left\{\frac{(2b_m+d)(d+f)^2}{\pi nd(2d+f)+(d+f)^2} - d\right\}^2 . \qquad (4\text{-}9)$$

With decreasing porosity corresponding to the increase of the number of screen layers in the wick, ϕ increases. It is assumed that the dependence of ϕ on ε can be expressed as follows ;

$$\phi = \phi_o + \phi_1 \varepsilon , \qquad (4\text{-}10)$$

where ϕ_o and ϕ_1 are constant.

For the flow in a slit channel which corresponds to the flow in the wick with n=0, the mean axial velocity is [2]

$$v_\ell = K_\ell (\Delta P_\ell - \rho_\ell g l \sin\psi)/(\mu_\ell l) , \qquad (4\text{-}11)$$

where $K_\ell = b_m^2/12$. (4-12)

On the other hand, K_ℓ for n= 0 is obtained from Eq.(4-9).

$$K_\ell = b_m^2/8\phi . \qquad (4\text{-}13)$$

From Eqs.(4-12) and (4-13), ϕ for ε =1 corresponding to n=0 is found to be 1.5. Then the following equation is obtained from Eq.(4-10).

$$\phi = \phi_o + (1.5-\phi_o)\varepsilon , \qquad (4\text{-}14)$$

where ϕ_o is the empirical factor which should be determined by experiment. From Eqs.(4-2), (4-9) and (4-14), the following equation is obtained.

$$K_\ell = \frac{1}{32\{\phi_o+(1.5-\phi_o)\varepsilon\}}\left\{\frac{(2b_m+d)(d+f)^2}{\pi b_m(2d+f)\frac{1-\varepsilon}{2}\cdot\frac{1-\varepsilon}{1-\varepsilon_m}+(d+f)^2}-d\right\}^2 . \quad (4-15)$$

In Section 3-8, the permeability K_ℓ is obtained as 2.4×10^{-10} m^2 by experiment with the potassium heat pipe, in the absence of the magnetic field. The porosity of the wick used in the experiment is 0.72, which is obtained from Eq.(4-2). Using these values, ϕ_o can be determined from Eq.(4-15), and then it is 14. Then the dependence of the permeability on the porosity can be calculated from Eq.(4-15) using 14 for ϕ_o.

A comparison between Eqs.(4-1) and (4-15) is shown in Fig. 4-2. It is revealed in this figure that the permeability of the loosely wrapped screen wick is higher than that of the tightly wrapped one. Furthermore, the permeability of the loosely wrapped screen wick shows a similar tendency to the case of the tight one. Equation (4-1) for the tight one is the semi-empirical equation based on many data under different mesh sizes, whereas equation (4-15) for the loose one is based on the value of ϕ_o, obtained from the specific structure of the wick.

So far, there are few data relating to the loosely wrapped screen wick. Then equation (4-15) is used for the estimation of the permeability in the following sections, though ϕ_o is determined by the experimental data relating to the specific structure of the wick. In future, equation (4-15) should be confirmed by experiments for various wick structures.

4-3 Influence of Wick Porosity on the MHD Effect

The Hartmann number can be obtained from Eq.(2-9) with reference to Eq.(4-15). The dependence of Ha on B is shown in Fig.4-3. The Hartmann number increases with the magnetic field strength under the given porosity in the wick. The dependence of Ha on $(1-\varepsilon)$ is shown in Fig.4-4. The Hartmann number increases with the porosity under a given field strength. In Fig.4-4, it is evident that the influence of the porosity on the Hartmann number is very large. As for B=0.5 Tesla, for instance, the Hartmann number in the wick with $\varepsilon=1$ is by two orders of magnitude higher than that in the wick with $\varepsilon=0.5$. The porosity corresponding to Ha=1 under B=0.5 Tesla is about 0.2, and decreases with increasing field strength.

The effect of the magnetic field on the flow can be regarded as the increase of the flow resistance in the wick. The increasing rate ζ due to the MHD effect depends on β and Ha.

In the heat pipe wick, β is expressed by Eq.(3-21). As shown in Eq.(3-21), β does not depend on the magnetic field strength but on the number of mesh screen layers and, accordingly, on the porosity of the wick. The dependence of β on $(1-\varepsilon)$ is shown in Fig.4-5, where the electrical conductivities of stainless steel and potassium were used for the calculation. As shown in this figure, β decreases with increasing porosity. However, the variation of β is by a few orders of magnitude lower than that of Ha under each field strength as seen in Figs.4-4 and-5. As for the dependence of ζ on B and ε, the variation of β can be neglected in comparison with that of Ha. Accordingly, it can be concluded that the effect of the magnetic field on the flow in the wick increases with the porosity as well as with the field strength.

Subsequently, the effective flow resistance, $R_f(B)$, in the magnetic field is estimated. The flow resistance can be calculated from Eq.(2-17) by using the evaluated values of permeability and the Hartmann number. The dependence of $R_f(B)$ on $(1-\varepsilon)$ under the various field strengths is shown in Fig.4-6. The effective flow resistance in the magnetic field decreases with the porosity in the wick increasing. Since the resistance in the magnetic field depends on the Hartmann number, the influence of the magnetic field on the resistance increases with the porosity as well as with the field strength.

4-4 Maximum Heat Transport Rate in the Magnetic Field

The maximum heat transport rate limited by the maximum wick pumping pressure in the magnetic field depends on the effective flow resistance. The maximum heat transport rate represents the heat transport capability of the heat pipe and then it should be increased as much as possible. To increase the maximum heat transport rate, the effective flow resistance should be decreased. From the viewpoint of the maximum heat transport rate, a large porosity of the wick is desirable for the heat pipe in the magnetic field (including the zero magnetic field). In addition, a large porosity is also desirable from the viewpoint of the liquid flow control by the magnetic field, since the MHD effect is considerable.

With increasing field strength, the maximum heat transport rate decreases. The influence of the magnetic field on the maximum heat transport rate will be considerable in the case of the wick which has a large porosity, since the effective flow resistance depends significantly on the field strength.

4-5 Concluding Remarks

The Hartmann number in the wick increases with increasing porosity of the wick as well as with the increasing field strength.

The effective flow resistance in the magnetic field decreases with increasing porosity in the wick. Under a given porosity, the effective flow resistance increases with the field strength. In the case of the wick which has a large porosity, the influence of the magnetic field on the effective flow resistance is very considerable. Then the maximum heat transport rate will significantly decrease with increasing field strength.

References

(1) Marcus, B. D. : NASA CR-2018 (1972).

(2) Bird, R. B. et al. : Transport phenomena.

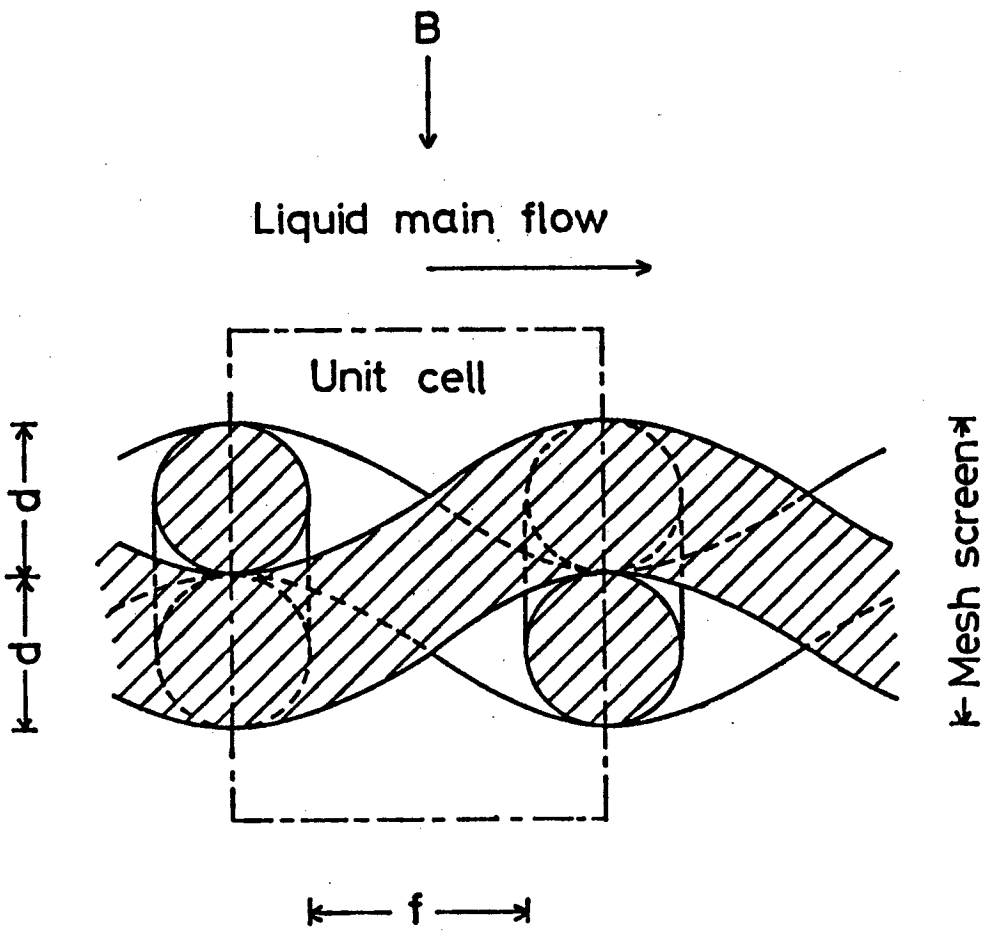

Fig.4-1 Details of mesh screen

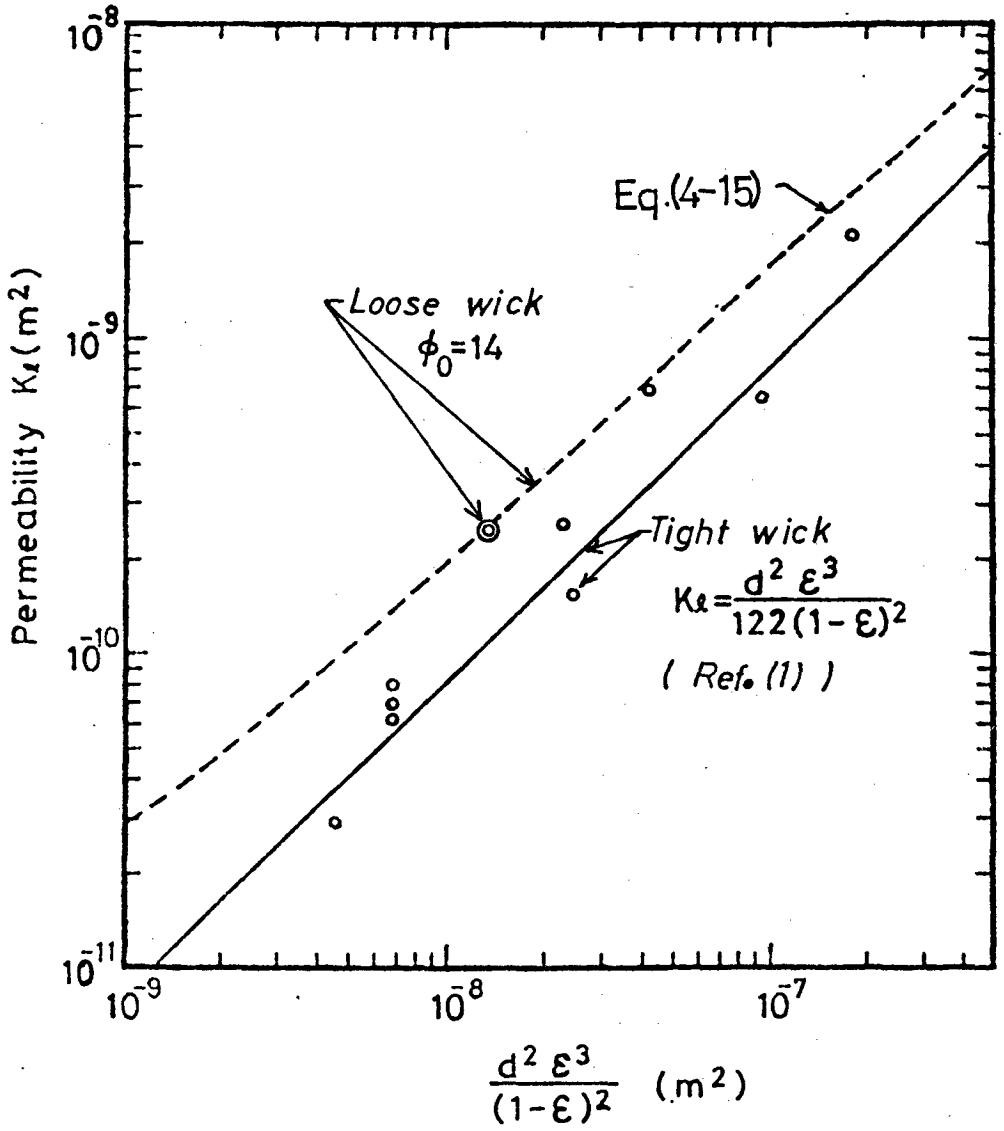

Fig.4-2 Comparison of the permeability between loose wick and tight one

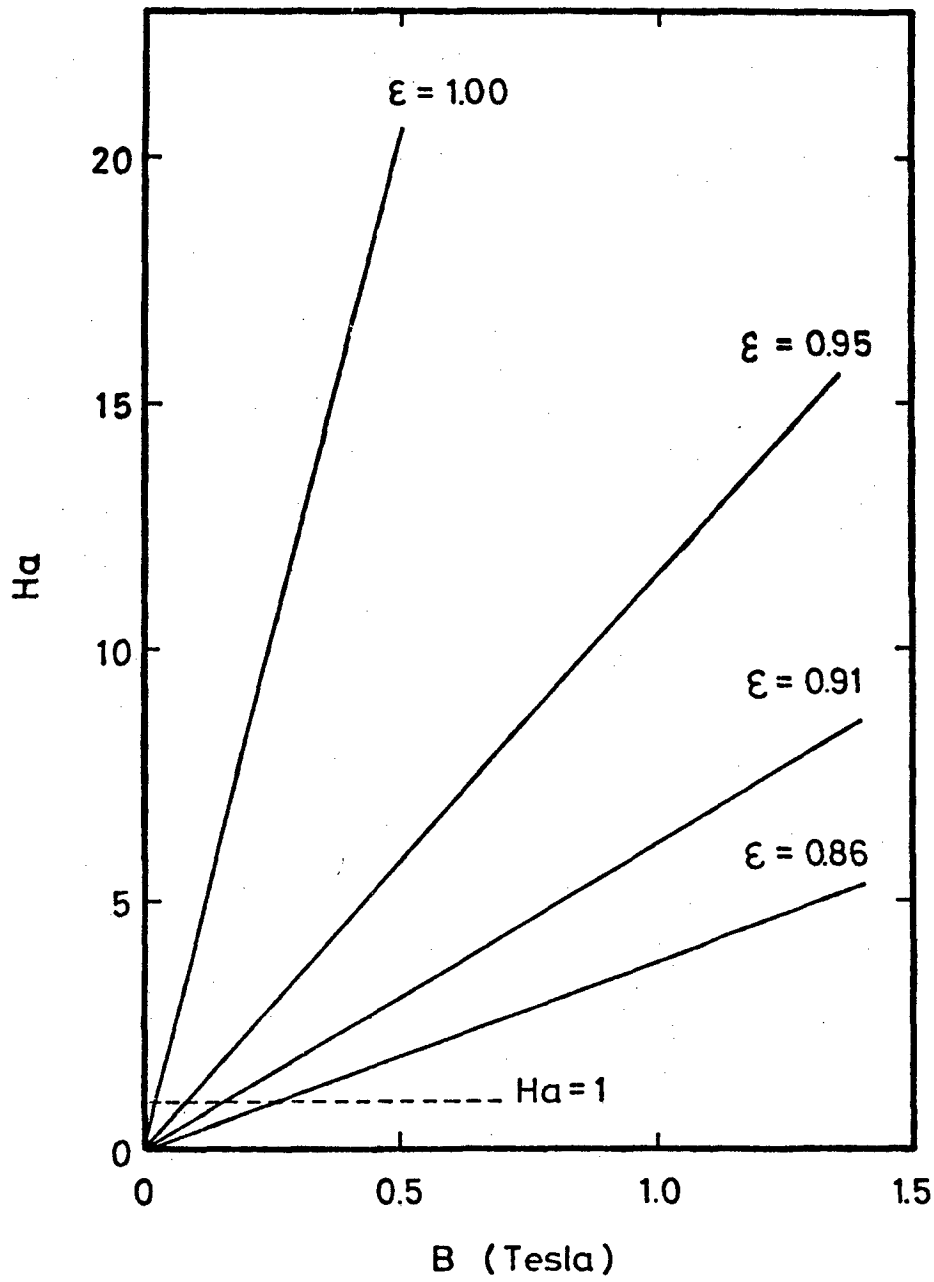

Fig.4-3 Ha vs B

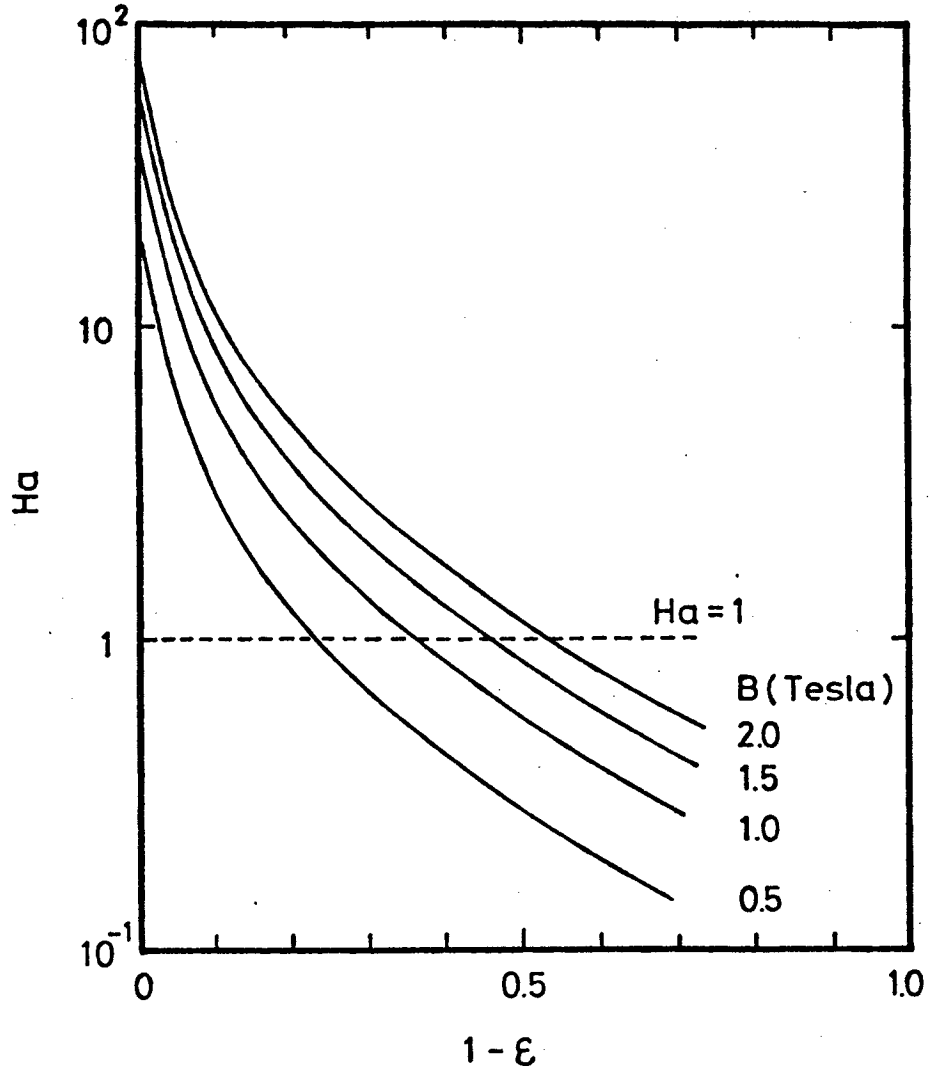

Fig.4-4 Ha vs. (1-ε)

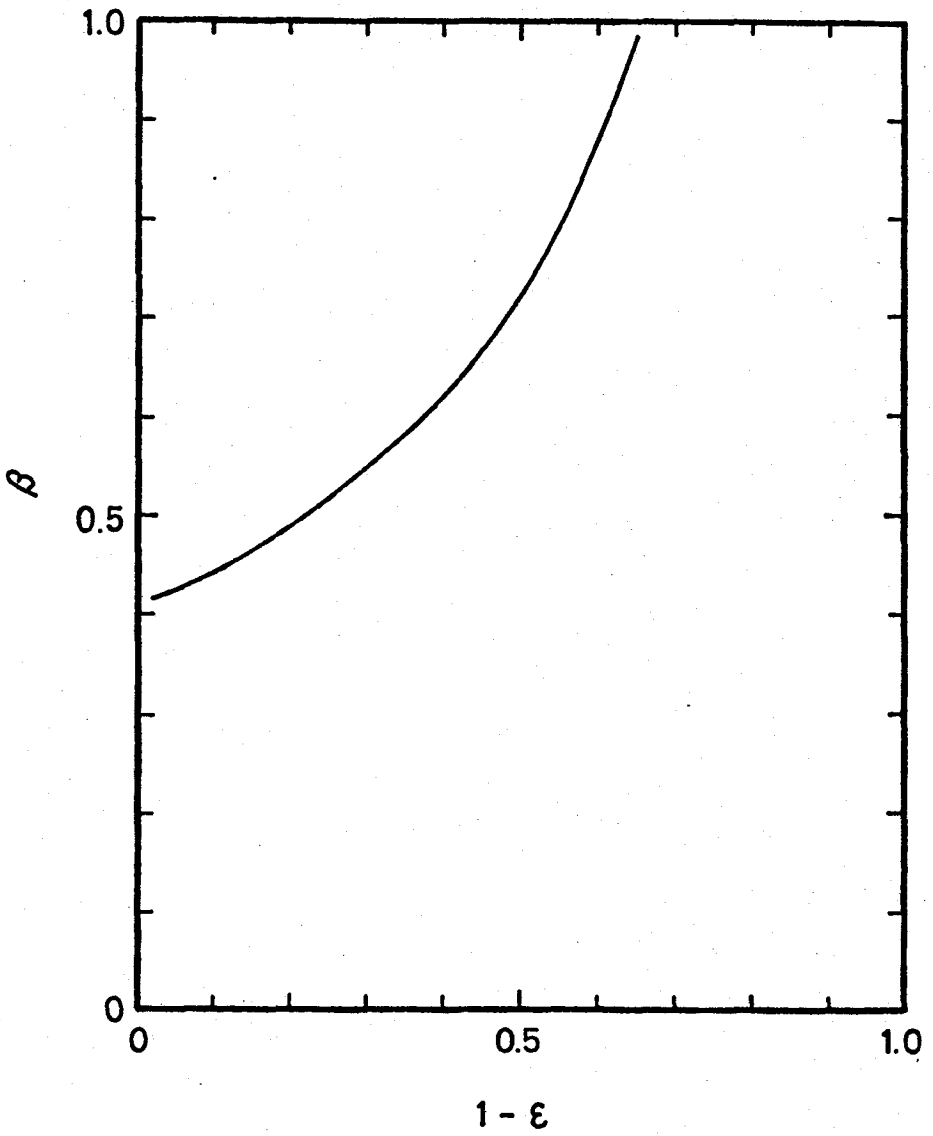

Fig.4-5 β vs. $(1-\varepsilon)$

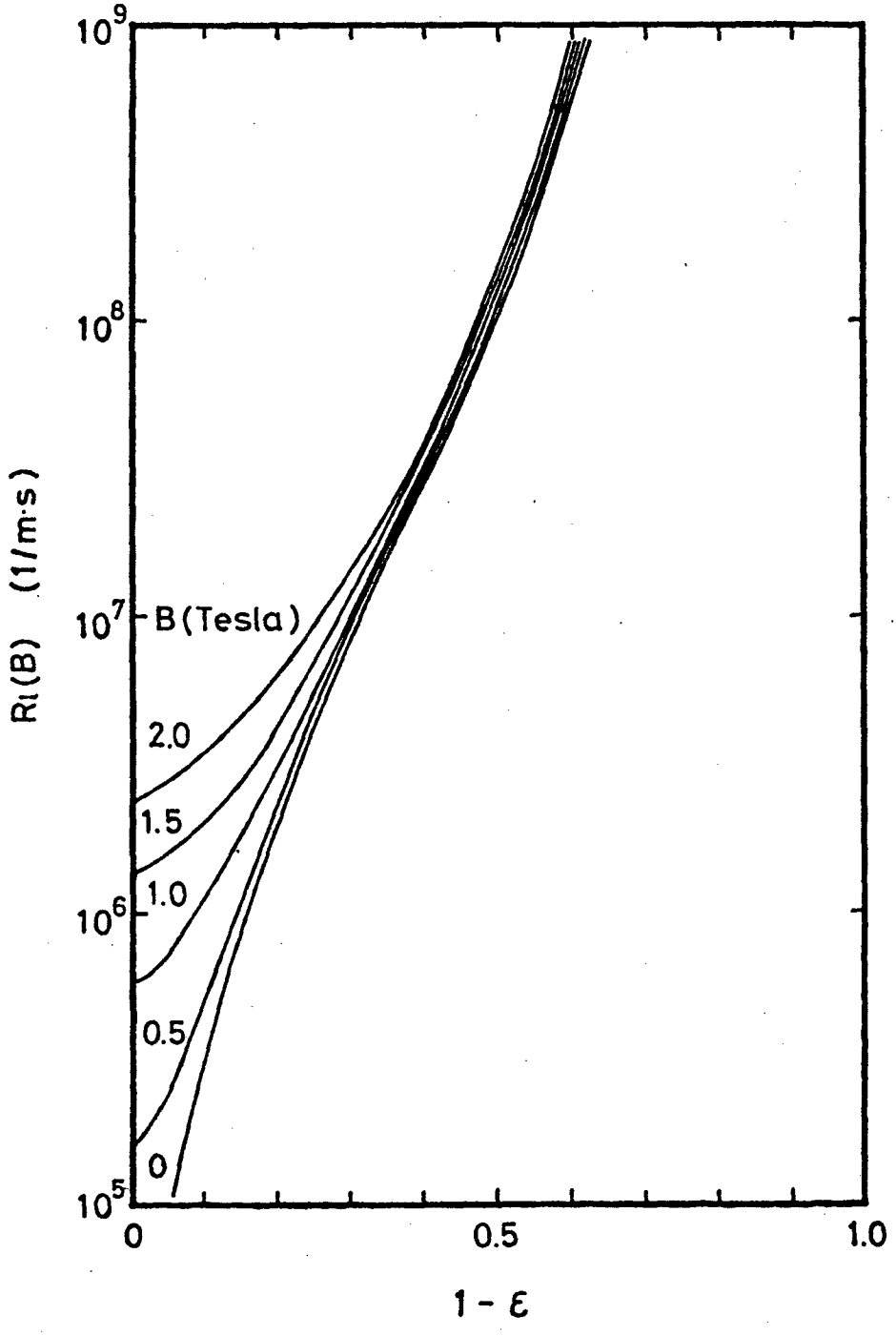

Fig.4-6 $R_{\ell}(B)$ vs. $(1-\varepsilon)$

Chapter 5.

Boiling Limit in the Magnetic Field

5-1 Introduction

In the evaporator section, the heat is transported across the wick to the vapor-liquid interface where the liquid is vaporized. Then the liquid in the wick is superheated by virtue of the curvature of the menisci and the radial temperature gradient. The greatest superheat in the wick exists at the interface of wick and container wall. With heat being added to the evaporator section, the superheat increases and becomes excessive, resulting in boiling within the wick. The influence of boiling on heat pipe operation depends on the nature of the wick used. If the vapor can escape the wick, the operation with boiling can be continued. If vapor cannot escape the wick, however, boiling leads the operation to failure. In this case, Marcus has proposed the equation of the radial heat flux limited by the boiling initiation, which is expressed as follows ;[1]

$$q_r = -k_{eff} \cdot \Delta T_s / b_m \ , \qquad (5\text{-}1)$$

where b_m is the thickness of the wick, k_{eff} is the effective thermal conductivity of the wick and ΔT_s is the temperature difference across the wick, between the vapor-liquid and the liquid-wall interfaces, which is equal to the incipient boiling superheat of liquid. Then the discussion on the boiling limit can be attributed to the discussion on the incipient boiling superheat of liquid.

In this chapter, the discussion is limited to the case that incipient boiling leads the operation to failure and the influence of the magnetic field on incipient boiling (IB) superheat of stagnant potassium is investigated, for the discussion of the boiling limit in the magnetic field.

5-2 Experimental Apparatus

The experimental apparatus of the test channel is schematically shown in Fig.5-1. The test channel was designed with the primary aim of measuring electromagnetic signals. It consists of a rectangular pipe made of AISI 304, with a 20x20 mm inner cross section and a wall 1 mm thick. It is filled with potassium up to a level of 270 mm from the bottom. A DC magnetic field is applied perpendicularly to the test channel so as to maximize the MHD effect.

The potassium is heated by an electric resistance heater wound on the channel wall, over a distance of 10 cm from the bottom.

The covering gas is exhausted from the test channel by a vacuum pump, and the pressure of the gas remaining in the channel is kept at a low level.

For measuring the liquid temperature, a thermocouple is immersed into the liquid inside the channel, while others are mounted along the outer wall to measure the axial distribution of temperature. For observing the movement of the liquid column and/or vapor bubbles, voltage taps are arranged along the channel wall at intervals of 1 cm, to measure the electric potential prevailing between two taps when a constant current of 10A is made to flow through the boiling test section. Also, an electromagnetic flow meter consisting of a permanent magnet with a field strength of 0.1 Tesla and measuring 45 mm in length is set across the channel to measure the velocity and acceleration of the potassium liquid column. A pressure transducer of strain gauge type is installed at the bottom of the channel for detecting pulses generated by condensation impact.

Signals from the thermocouples are fed to pen recorders, and those from the voltage taps and the flow meter to a magnetic tape recorder of 14 channels.

5-3 Experimental Results

Typical transient signals registered upon initiation of boiling without magnetic field are shown in Fig.5-2(a). The signals from the potential taps and from flowmeter evidence single slug ejections taking place intermittently. Transient signals with magnetic field are shown in Fig.5-2(b).

The pattern of the signals emitted upon boiling initiation is quite different, due to the MHD restraint applying on the motion of the liquid column above the vapor bubble. After boiling inception, boiling continues to be discerned for several seconds from the voltage tap readings as shown in Fig.5-2(b) while the potassium temperature indicated by T1 remains almost constant.

The axial position of the boiling initiation is determined from voltage tap readings, which indicates that the boiling takes place beyond a distance of 4 to 6 cm from the bottom of the channel or about midway along the heated section. This position is near the location of the thermocouple T1 immersed in the liquid. No detectable change is observed in the position of the boiling initiation whether the magnetic field is present or absent. Hence the temperature change of T1 upon boiling initiation is nearly equal to IB superheat of potassium at the position of boiling initiation.

The relation between the degree of IB superheating ΔT_{sat} and the magnetic field strength B is shown in Fig.5-3. Each plot in this figure represents the average of about ten measurements, and the bars indicate the standard deviation. It is revealed that IB superheat is not meaningfully influenced by the strength of the magnetic field.

Measurements of IB superheat were performed under different conditions of heating, either parallel (case A) or perpendicular (case B) to the magnetic field, and a comparison was made between the cases A and B. In these runs, two pairs of heaters were arranged symmetrically on opposite sides of the channel wall, one pair to heat the channel wall parallel, and the other pair perpendicular, to the magnetic force lines.

If nucleation cavities are assumed to have their axes at right angles to the channel wall, the liquid in such cavities would cut across the magnetic field in its movement induced by the fluctuating liquid pressure, and would thereby be subjected to the MHD force when the channel walls parallel to the magnetic field are heated, while conversely heating only of the walls perpendicular to the magnetic field should leave the liquid free from the MHD effect. Actually, the cavities may not necessarily be oriented perpendicularly to the channel wall, but it could still be expected that a sufficiently strong MHD effect on the motion of the liquid in the wall cavities should produce an appreciable difference in IB superheating between cases of different magnetic field axing. Table 5-1 presents the data actually obtained for the two modes of heating. No meaningful difference can be discerned between the two cases of magnetic field axing.

5-4 Discussion

The effect of the magnetic field on nucleation in wall cavities is considered. Nucleation models proposed so far can be classified into two categories; static and dynamic.

The first named model considers IB superheat from the thermodynamic equilibrium prevailing between the liquid at rest and vapor and/or gas present in wall cavities. Most current nucleation models can be included in this group. With this model, the magnetic field would not affect void nucleation, and would only influence bubble growth after boiling inception, because the MHD effect would affect the liquid only when it travels across the magnetic field. Thus, when the static model is adopted, IB superheat must be considered to be independent of the magnetic field. Hence, if a functional relationship between the magnetic field and IB superheat is to be considered, this should require treatment by a dynamic model such as described below.

The triggering mechanism that initiates boiling of superheated sodium has been identified by Bankoff[2] with random pressure fluctuations due to flow turbulence, while resonance with pressure oscillations occurring in the vapor in wall cavities has been proposed by Smidt.[3] In this connection, if the motion of the liquid in the wall cavity has a component perpendicular to the magnetic field, this liquid would be subjected to MHD interaction. This circumstance would relate IB superheat to the magnetic field.

The two authors cited above have shown that the liquid pressure in a wall cavity is dependent on time t. If a wall cavity such as shown in Fig.5-4 is considered as a model, the motion of liquid in this cavity is expressed by [3]

$$\frac{\rho_\ell l}{\pi r_1^2}\frac{d^2V}{dt^2} + \frac{8\mu_\ell l}{\pi r_1^4}\frac{dV}{dt} + \frac{2\gamma}{r_2}\frac{Con.}{\pi r_2^3}(V-V_1) = -p(t) , \qquad (5\text{-}2)$$

where Con. is a constant. In a magnetic field it is necessary to consider the MHD effect on the liquid motion.

$$\frac{\rho_\ell l}{\pi r_1^2}\frac{d^2V}{dt^2} + \left(\frac{8\mu_\ell l}{\pi r_1^4} + \frac{\beta\sigma_\ell B^2 l}{\pi r_1^2}\right)\frac{dV}{dt} + \frac{2\gamma}{r_2}\frac{Con.}{\pi r_2^3}(V-V_1) = -p(t). \qquad (5\text{-}3)$$

When $\beta=1$, B=0.7 Tesla and $r_1=3\times10^{-6}$ m, the Hartmann number defined as the ratio between the MHD term and that of friction is expressed by

$$Ha^2 = \beta\sigma_\ell B^2 l/(8\mu_\ell l/r_1^2) = 1/300 . \qquad (5\text{-}4)$$

This indicates that the MHD effect is negligible when compared with the friction term, under the conditions adopted in the present experiment. The term representing the MHD effect would become comparable with that of friction only when, say, B>13 Tesla.

The transfer function between pressure pulsations and the fluctuations of liquid can be obtained by Laplace's transformation of Eq.(5-3) ;[3]

$$G(\omega)^2 = (1/a_1^2)/\{(\omega^2-\omega_o^2)^2 + 4a_o^2\omega_o^2\omega^2\} ,$$

where

$$a_o = a_2/(2\omega_o a_1),\ a_1 = \rho_\ell l/(\pi r_o^2),\ a_2 = \frac{8\mu_\ell l}{\pi r_1^4} + \frac{\beta\sigma_\ell B^2 l}{\pi r_1^2}. \qquad (5\text{-}5)$$

The resonance angular frequency ω_o is 4×10^5 sec^{-1} [3]. The angular frequency ω of the pressure pulsation due to natural circulation in the liquid contained in the test equipment would be much smaller than ω_o (e.g., $\omega=10^3$ for forced flow water, according to Kadlec et al.[4]). Thus the transfer function is almost independent of a_o representing the MHD effect, and even an intense magnetic field of, say, 10 Tesla, would scarcely have any effect on the resonance cavity.

If the influence of the magnetic field on boiling initiation is limited to the MHD effect on liquid motion in the wall cavity, and the mechanism of the boiling initiation can then be described by Eq.(5-3), it follows that IB superheat is not influenced by the magnetic field.

5-5 Concluding Remarks

Nucleation in the wall cavity is not influenced by the MHD force, which is negligible relative to the frictional force, hence IB superheat is not influenced by the magnetic field. From the viewpoint of IB superheat it is concluded that the boiling limit is not influenced by the magnetic field.

If, however, the radial heat flux is not limited by the boiling initiation, the above conclusion is not applicable. In this case, the problem becomes very complicated since the liquid flow depends on the behavior of the vapor bubble in the wick. Then the critical radial heat flux cannot be predicted except by empirical means.

References

(1) Marcus, B. D. : NASA CR-2018 (1972).

(2) Bankoff, S. G. : Int. Seminar on Heat Transfer in Liquid Metals, Yugoslavia, Paper 28 (Sept. 1971).

(3) Smidt, D. : 4th LMBWG Karlsruhe.

(4) Kadlec, J., Appelt, K. D. : Nucl. Eng. Design, 14, p136 (1970).

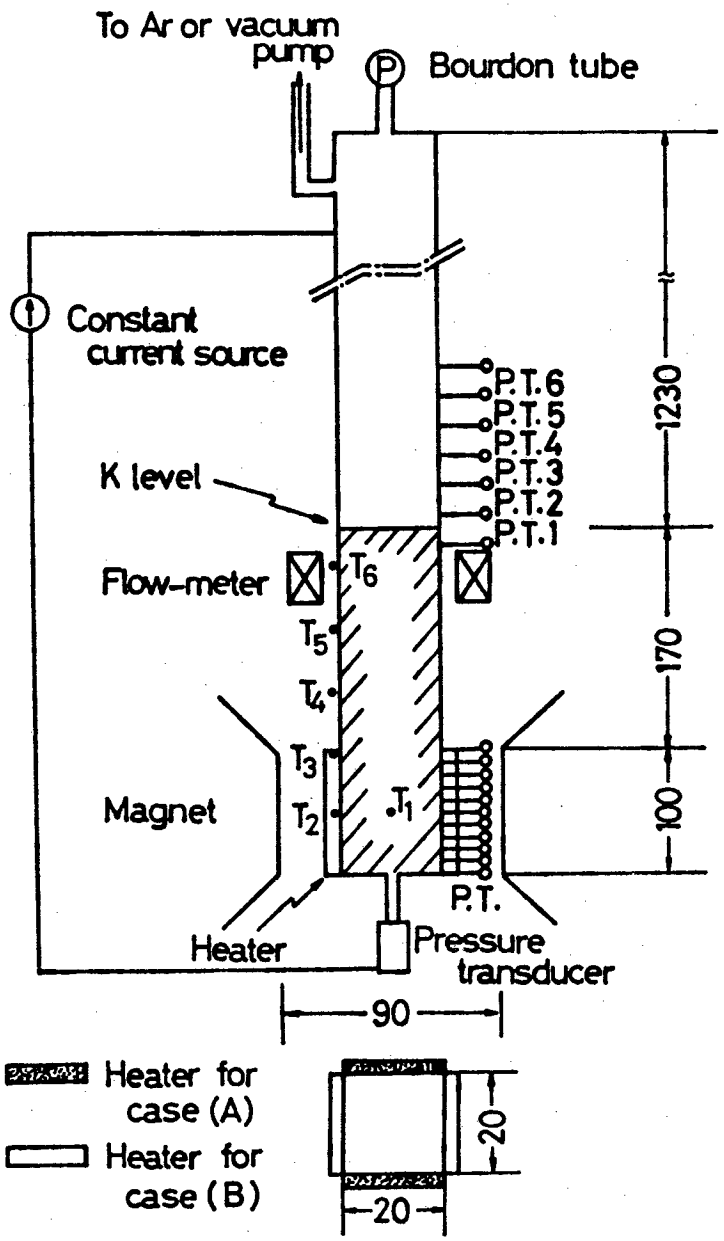

Fig.5-1 Schematic diagram of experimental apparatus

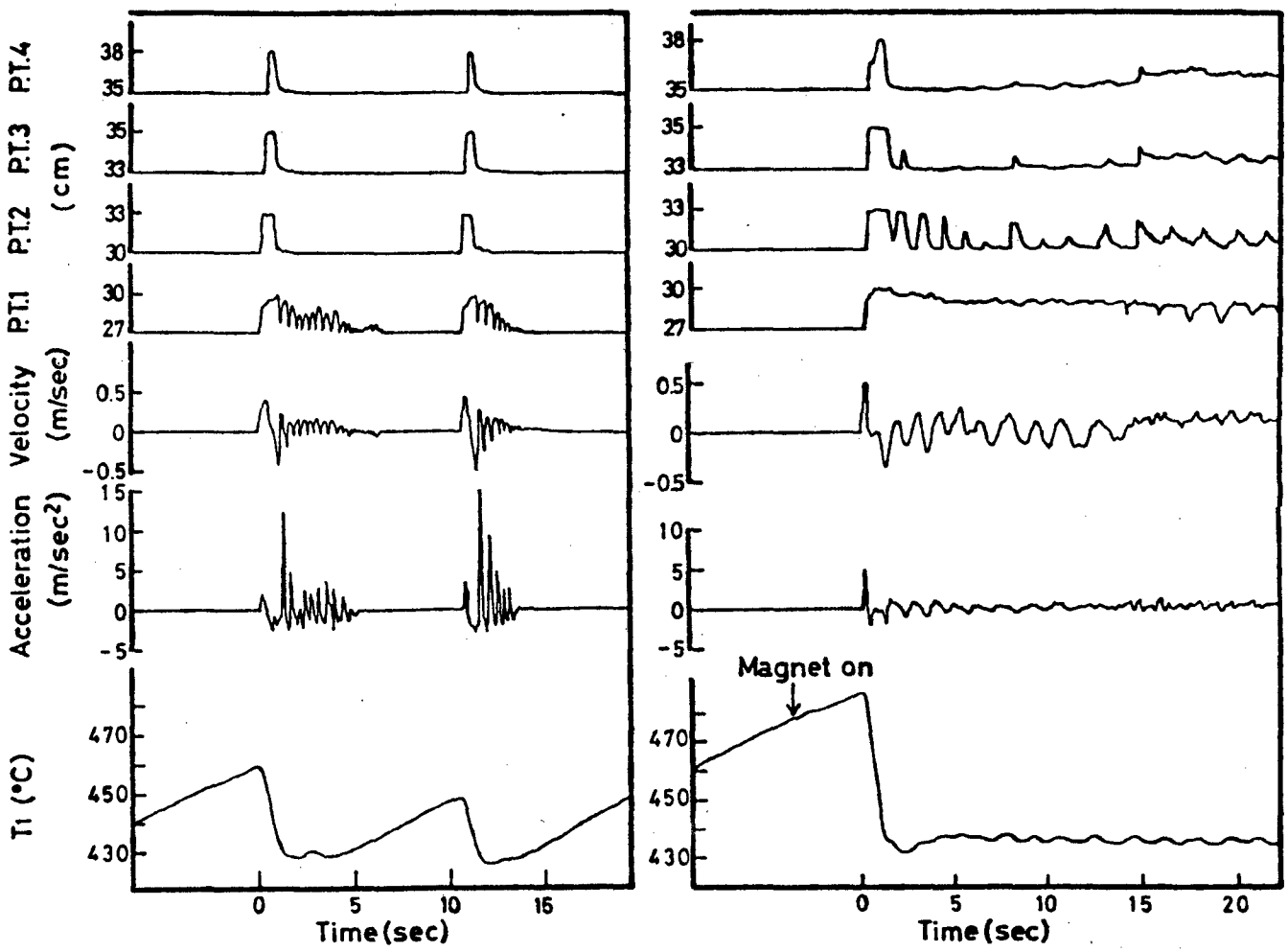

(a) Absence of magnetic field (b) Presence of magnetic field (B=0.7 Tesla)

Fig.5-2 Transient signals at boiling initiation

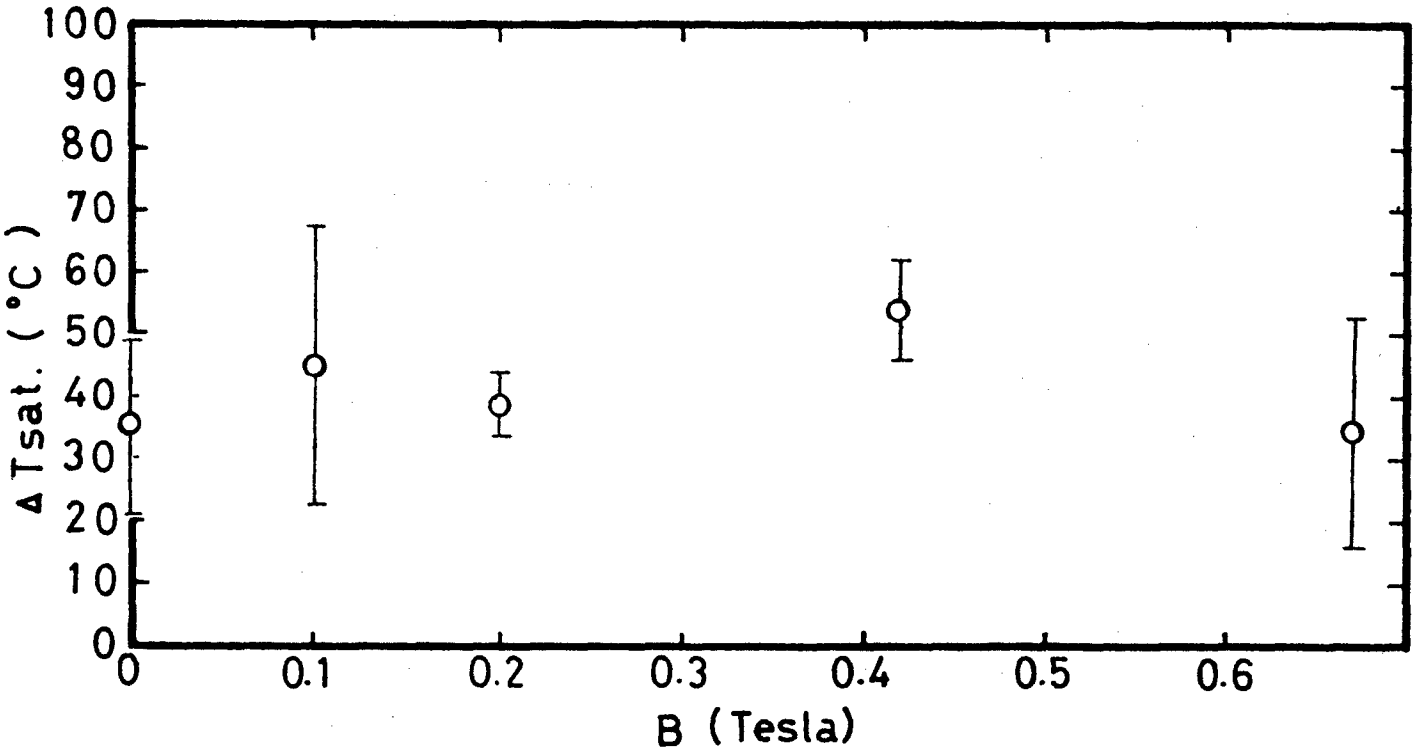

Fig.5-3 IB superheat vs. magnetic field strength

Table 5-1 Comparison of IB superheat in Cases A and B

B(Tesla)		Q=600 W		Q=400 W	
		Case A	Case B	Case A	Case B
0	Av.	84.4	94.2	72.3	76.8
	σ	9.2	38.5	20.9	29.0
0.1	Av.	121	96.2	87.4	87.8
	σ	39	21.7	28.6	13.2
0.4	Av.	97.3	106	46.0	54.2
	σ	33.3	23	9.2	17.0

Av. : Average, σ : Standard deviation

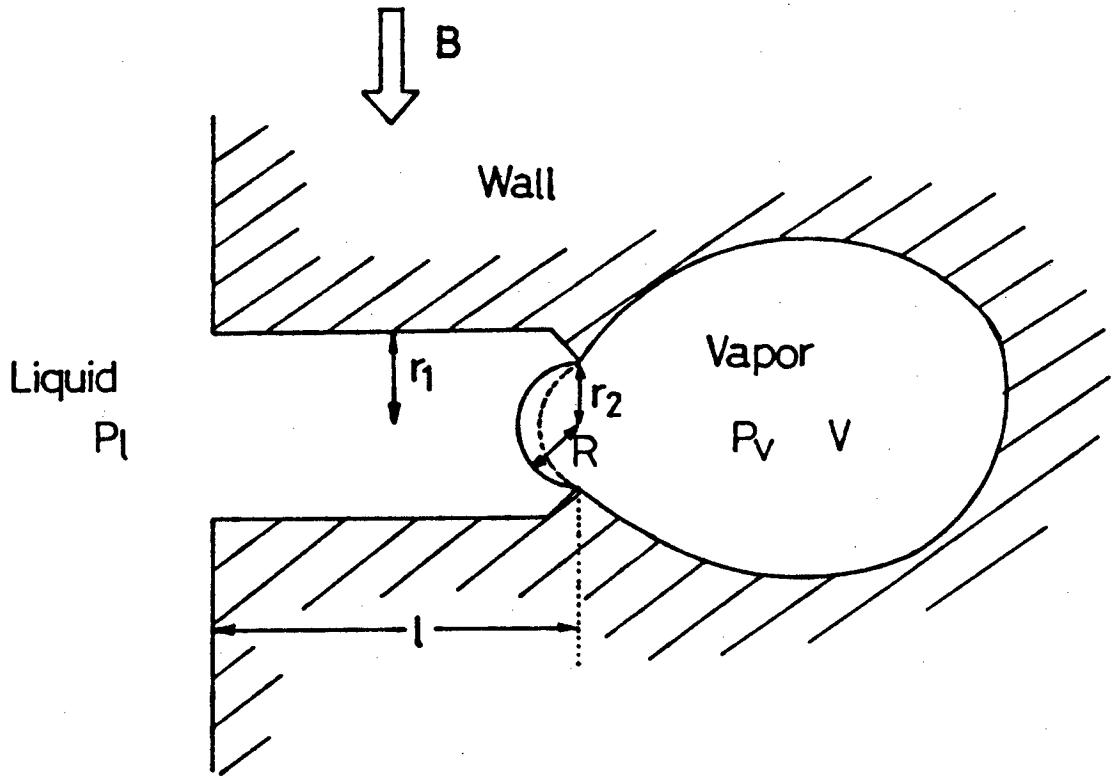

Fig.5-4 Schematic diagram of wall cavity model

Chapter 6.

Influence of Inert Gas on Heat Transport Characteristics of Potassium Heat Pipe

6-1 Introduction

In the experiment described in Chapter 3, it is presumed from the axial temperature distribution that a small amount of non-condensable gas might be present in the heat pipe. Since the experiment of the sodium heat pipe performed by Grover,[1] many investigators are encountering the problem of gas existing in the heat pipe. As for the liquid metal heat pipe, especially, it is well known that the gaseous impurities are liable to mix in the container because of its high operating temperature. The heat transport characteristics of the heat pipe in the magnetic field, as described in Chapter 3, would be influenced by the gas. Then the influence of the gas on the heat transport characteristics should be discussed.

In this chapter, the influence of inert gas on the heat transport characteristics of potassium heat pipe is experimentally studied over a wide range of gas loaded in the zero magnetic field. Observations are made on the Q-T characteristics, on the axial temperature distribution and on the thermal conductance of the heat pipe. Furthermore, the influence of the inclination ψ on thermal conductance is investigated with the parameter of gas loaded, for a discussion on the influence of the body force acting on the liquid flow in the wick.

6-2 Experimental Apparatus and Procedure

The structure of a potassium heat pipe,used in the present experiment,is shown in Fig.6-1. The wick structure and the working fluid for the heat pipe are the same as in the previous experiment described in Chapter 3, but the heat pipe has a circular cross section. Chromel-alumel thermocouples sheathed in stainless steel tubing of 1.0 mm O.D. are arranged on the outer wall of the container at the positions marked T5~T12, and the same thermocouples labeled T1~T4 are inserted into the vapor space. These thermocouples in the container are attached to the thin stainless steel rod of 2.0 mm O.D. stretched between both end caps of the container. On the outer wall of the cooled section a cooling jacket is installed and a copper tube of 8.0 mm O.D. is closely wound on the jacket wall. The heat is removed by cooling water flowing through the jacket and coils. Depending on the purpose of the experiment, air is sometimes filled into the jacket instead of flowing water, to vary the thermal conductance by changing its pressure. In this case, the heat is transported through the air jacket and indirectly removed by water flowing through the coils.

Prior to the experiment, the heat pipe container and the gas reservoir are cleaned. The cleaning process includes repeated washing by acetone and drying several times. After drying, the heat pipe container is exhausted for ten hours at 500 ^{o}C. After the cleaning process, potassium is loaded into the heat pipe in an argon atmosphere. Subsequently, argon is exhausted up to 10^{-6} Torr by a vacuum pump, and a trial run is performed for three days, for the purpose of removing gaseous impurities from the working fluid.

In the experiment, argon is filled into the heat pipe, and the initial gas pressure is measured by the manometer installed at the gas reservoir. The amount of argon loaded is regulated by valves of a gas-filled bomb, and a vacuum system is connected to the gas reservoir. After that, the heat is added to the evaporator section in an electrical furnace by radiation from the siliconit pyrogen unit of the double spiral tube type, and the cooling water is introduced to the cooling section. The mass flow rate of cooling water is controlled by a regulator and kept constant. The electrical power supply to the furnace is controlled for the regulation of the furnace temperature and the heat addition to the heat pipe is varied by changing the furnace temperature.

The heat pipe is inclined to examine the influence of gravity on the heat transport of the heat pipe. Most of the runs were performed with the evaporator position above the condenser section.

The loaded amount of argon ranged in initial pressure from 10^{-2} to 10^{2} Torr at room temperature.
The heat transport rate was evaluated from the mass flow rate, and from the temperature difference of cooling water. The temperature signals were recorded by a multi-pen recorder.

6-3 Transient Behavior of Potassium Heat Pipe without Gas Loading during Trial Run

The transient behavior of potassium heat pipe during the trial run before the gas loading experiment is shown in Fig.6-2, where Q is the heat removal rate in the condenser section, T_v the vapor temperature in the evaporator section and T_{co} the temperature of the cooling water. The results were obtained by measuring the transient start-up data of the vapor temperature and the heat removal rate under the constant furnace temperature. As revealed in this figure, the heat pipe operating condition, being represented by $Q/(T_v - T_{co})$, reaches its steady condition within about one hour, and after that it is constant.
Normally, no gaseous impurities are produced in the heat pipe after the trial run, but even if such gas is produced after the run, its influence on the operating conditions is negligible.

6-4 Heat Transport Characteristics of Argon-Loaded Potassium Heat Pipe

In this section, the heat transport characteristics of the argon-loaded potassium heat pipe will be discussed. The change of the axial temperature distribution during start-up is shown in Fig.6-3, where the loading amount of argon is represented by the initial gas pressure P_{gi} before start-up at room temperature. The results were obtained by increasing the heat addition in discrete steps, under a constant initial gas pressure P_{gi} of argon, the constant air pressure P_j in the air jacket installed on the container wall of the cooling section, and the constant mass flow rate M_{co} of cooling water, and after each step, the temperatures along the heat pipe axis were allowed to reach steady condition before measurements were taken. This way of stepwise start-up is called "slow start-up".[2] In Fig.6-3 it is revealed that the sharp temperature gradients are present in the condenser section and that the position where the sharp temperature gradient appears, shifts downstream with the increasing furnace temperature T_f. From the temperature profiles, it is presumed that the gas is swept along and accumulates in the condenser section, impeding the vapor flow.

Q-T characteristics of the argon-loaded potassium heat pipe during the slow start-up are shown in Fig.6-4.

As seen in this figure, the heat transport rate is much lower than the theoretical sonic limited heat transport rate Q_s, which is obtained from Levy's equation.[3]

$$Q_s = \rho_v v_{vs} \lambda A_v / \sqrt{2(\kappa+1)} \quad , \tag{6-1}$$

where v_{vs} is the sonic velocity of vapor and κ is the ratio of specific heat. Equation (6-1) is based on the assumption that the shear stress can be ignored. This assumption causes a higher heat transport rate. However, it is a most convenient equation because it allows a direct calculation of the sonic limit in terms of vapor conditions which are easily determined. From Eq.(6-1), the following equation is obtained.

$$Q_s = \lambda P_v A_v \sqrt{\kappa / \{ 2P_v(\kappa+1)T_v \}} \quad . \tag{6-2}$$

The sonic limiting curve in Fig.6-4 is calculated by Eq.(6-2), where the relation between vapor pressure P_v (atm) and temperature T_v (^{o}K), used in a saturated condition, is written as follows ;[5]

$$\log_{10} P_v = 6.59817 - 4625.3/T_v - 0.700643 \log_{10} T_v \quad . \tag{6-3}$$

From the presumption in Fig.6-3, it can be considered that the reduction of the heat transport rate is caused by the presence of inert gas accumulating in the condenser section.

Actually, the gas covers a portion of the condenser section and impedes vapor flow and condensation, resulting in the decrease of the effective area of vapor condensation. The dependence of the heat transport rate on the thermal conductance in the cooling section is also discussed on this presumption. According to Fig.6-4, the heat transport rate is insensitive to the variation of air pressure P_j in the air jacket of the cooling section in the region of the low vapor temperature, because the argon covers the whole area of the cooling section in the low vapor temperature region. Hence the thermal conductance along the vapor flow through the accumulating argon is much smaller than that in the air jacket of the cooling section, and the heat transport rate is scarcely influenced by the change of conductance in the air jacket. Then, with the removal of argon from the cooling section to the reservoir section, the heat transport rate becomes sensitive to the conductance in the air jacket of the cooling section. In Fig.6-3, the argon is swept and compressed toward the reservoir section with the vapor temperature in the evaporator section increasing corresponding to the increase of the furnace temperature, and simultaneously, in Fig.6-4, the heat transport rate increases and becomes sensitive to the conductance in the air jacket with the vapor temperature increasing. These results show that inert gas accumulating in the condenser section has an effect on the heat transport rate as well as on the temperature distribution.

6-5 Dependence of Over-All Thermal Conductance on Initial Gas Pressure

In this section, the influence of initial gas pressure on over-all thermal conductance of the potassium heat pipe will be discussed. Figure 6-5 shows the temperature distribution along the axis of the heat pipe under different initial gas pressure conditions, but at the constant heat transport rate. In this figure, the heat was directly removed by cooling water flowing through jacket and coils, and the mass flow rate of cooling water M_{co} was kept constant. It is revealed in the figure that the vapor temperature T1 in the evaporator section decreases, and that the sharp temperature gradient is reduced with decreasing initial gas pressure P_{gi}. It is said that an over-all thermal conductance of the heat pipe increases with decreasing P_{gi}, since the vapor temperature in the evaporator section decreases at the constant heat transport rate.

Now, we define the over-all thermal conductance U_o of the heat pipe as follows ;

$$Q = U_o(T_v - T_{co}) \ , \qquad (6\text{-}4)$$

From the definition, the over-all thermal conductance U_o depends on the thermal conductance along the heat flow path ; vapor flow through the adiabatic section to the condenser section, condensation of vapor, conduction in the wick and wall, and heat transfer to the cooling water.

From Eqs.(6-2) and (6-4), the thermal conductance U_s corresponding to the sonic vapor flow can be obtained by using Q_s for Q and U_s for U_o in Eq.(6-4).

$$U_s = \lambda P_v A_v \sqrt{\kappa / \{2R_v(\kappa+1)T_v\}} / (T_v - T_{co}) \ . \qquad (6\text{-}5)$$

Figure 6-6 shows the dependence of U_o on P_{gi} at the constant heat transport rate of 300 W. It is revealed in the figure that the over-all thermal conductance U_o of the heat pipe gradually increases and approaches to that corresponding to the sonic vapor flow with decreasing P_{gi}.

For discussing the dependence of U_o on P_{gi} in more detail, let us compare the experimental results with the theoretical values obtained from the flat-front model. Figure 6-7 shows the axial temperature distribution in the flat-front model, which is based on the assumption that the vapor-gas interface between the active and the gas-plugged portions of the heat pipe is very sharp, and that the pressure drop in vapor flow is negligible. On this assumption, the heat transport rate in the flat-front model can be expressed as follows ;[6]

$$Q = h l_p (T_v - T_{co}) \left(l_c + \frac{V_r}{A_v} - \frac{P_{gi} V_o}{A_v P_v} \right) , \qquad (6\text{-}6)$$

where h is the coefficient of heat transmission and l_p is the perimeter of the heat pipe container, and where the vapor pressure corresponding to T_{co} in the gas-plugged region is neglected.

From Eq.(6-4), and by using U_f for U_o, the conductance U_f corresponding to the flat-front model is

$$U_f = Q/(T_v - T_{co}) \ , \tag{6-7}$$

where T_v is the vapor temperature in a saturated condition, corresponding to P_v. From Eq.(6-6), the thermal conductance U_f is related to the initial gas pressure P_{gi} under the given operating temperature T_v and the heat transport rate Q.

$$P_{gi} = \frac{P_v}{V_o}\left(A_v l_c + V_r - \frac{A_v}{h l_p}\frac{Q}{T_v - T_{co}}\right) \ . \tag{6-8}$$

Usually, the condenser section expands into the portion of the adiabatic section due to the axial heat conduction in wick and wall at the end of the cooling section, and the way of taking the value of the axial length l_c of the condenser section is a problem in the calculation of U_f. However, since U_f depends weakly on l_c, it is sufficient for the calculation of U_f to take the nominal length of the cooling section as the value of l_c in Eq.(6-8). As for the evaluation of h, it is sufficient to consider only the heat conduction in wick and wall since the thermal resistance corresponding to the heat conduction is much larger than the resistance between wall and cooling water. Accordingly, the thermal conductance U_f can be calculated from Eqs.(6-7) and (6-8), as represented by the solid curve in Fig.6-6.

As seen in Fig.6-6, the experimental results are in good agreement with the theoretical values obtained from the flat-front model in the region of the high initial gas pressure. With decreasing P_{gi}, however, the results deviate from the theoretical curve. For the discussion, the deviation is written in the form of thermal resistance as follows ;

$$1/U_d \equiv 1/U_o - 1/U_f \ , \qquad (6\text{-}9)$$

and the ratio between U_s and U_d is represented by ξ.

$$\xi = U_s(1/U_o - 1/U_f) \ . \qquad (6\text{-}10)$$

When the over-all thermal conductance of the heat pipe can be described with the flat-front model, ξ takes the value of zero, and when the conductance is limited by the sonic vapor flow, ξ takes the value of unity. And the change of ξ from zero to unity corresponds to the transition of U_o from U_f to U_s. The dependence of ξ on P_{gi} is shown in Fig.6-8, where the solid curve is calculated by using the following formula for approximation ;

$$\xi = 1 - (P_{gi}/P)^n \ , \qquad (6\text{-}11)$$

where index n and pressure P are chosen to fit the experimental data. The same values of n and P are used to calculate the dotted curves in Fig.6-6 for fitting the data. Equation (6-11) is used for the extrapolation of U_o in the next section.

It is revealed in Fig.6-8 that the value of ξ increases from 0 to 1 with decreasing P_{gi}.

As for the dependence of the axial temperature distribution on ξ , it is seen from Fig.6-5 that the steep temperature distribution corresponding to the flat-front model becomes gradual and approaches that characterized by the sonic vapor flow with increasing ξ, corresponding to the decrease of P_{gi}. From the change of the temperature distribution, the thermal conductance in each section is discussed. The increase of the temperature difference suggests the decrease of the thermal conductance at that section, and vice versa. In Fig.6-5, the axial temperature difference between T1 and T10 is increased, while the difference between T10 and T4 is decreased with decreasing P_{gi}. Then it is said that the thermal conductance U_a along the evaporator and the adiabatic sections decreases, but that the conductance U_c in the condenser section increases with increasing ξ corresponding to the decrease of P_{gi}. However, the increase of U_c is larger than the decrease of U_a, and then, the over-all thermal conductance U_o gradually increases as shown in Fig.6-6. In the case of the flat-front model condition, U_a is much larger than U_c ($U_c=U_f=U_o$), whereas the relation is reversed in the case of the sonic vapor flow condition ($U_a=U_s=U_o$), and the decrease of P_{gi} raises U_c and reduces U_a, but increases the over-all thermal conductance U_o.

The increase of ξ is caused by both influences of decreasing U_a and increasing U_c. Then ξ increases from zero with decreasing P_{gi} and approaches unity.

6-6 Influence of Gravitational Force on Over-All Thermal Conductance

In this section, the influence of the gravity on the over-all thermal conductance U_o is discussed. The Q-T characteristics of the potassium heat pipe under various angles ψ of inclination, but at a constant initial gas pressure P_{gi} and a constant mass flow rate M_{co} of cooling water, are shown in Fig.6-9, where the experimental data were obtained in the way of increasing furnace temperature by steps and measuring the heat removal rate and the evaporator temperature under steady conditions, with the angle of inclination being kept constant at each step. Each of the dotted lines in Fig.6-9, shown with the straight line, follows the experimental data of each angle of inclination, therefore the line represents the Q-T line, with P_{gi}, ψ and M_{co} remaining constant. The solids in Fig.6-9 represent the data just before the abrupt temperature rise in the evaporator section, i.e. the dry-out. The maximum heat transport rate limited by the maximum wick pumping pressure depends on the angle of inclination, and usually it is measured from the wick dry-out. In Fig.6-9, the heat transport rate, just before the wick dry-out, actually depends on the angle of inclination.

Then, the heat transport rates represented by the solids are the maximum heat transport rates limited by the maximum wick pumping pressure.

As seen in Fig.6-9, the Q-T line shifts in parallel toward a lower region of the heat transport rate, with the angle of inclination increasing. Then, it is said that not only the maximum but also the heat transport rate corresponding to the same vapor temperature is decreased with the angle of inclination. The results show a similar tendency in Fig.3-4. Using the relation (3-9), the influence of the gravitational force on the heat transport rate is discussed. In Fig.6-9, the difference of the heat transport rate corresponding to the same vapor temperature at any Q-T point between the cases of ψ_1=5 and ψ_2=15 deg. is 210 W, and the difference between the cases of ψ_1=5 and ψ_3=25 deg. is 400 W. Then, the ratio between these values is 0.53, while the value obtained from the right-hand side in Eq.(3-9) is 0.51. From the good agreement between the values, it is found that the decrease of the heat transport rate corresponding to the same vapor temperature is caused by the reduction of the wick pumping ability imposed by the gravitational force, without any change of the wick pumping pressure $\Delta P_{\ell o}$. In addition, it is seen in Fig.6-9 that the decrease of heat transport rate corresponding to the same vapor temperature at any Q-T point is equal to the difference between the maximum heat transport rates represented by the solids.

This agreement shows the validity of the above discussion of the effect of the gravitational force. The experimental results in Fig.6-9 show that the wick pumping pressure is only a function of the operating temperature and does not depend on the body force acting on the liquid flow in the wick.

Subsequently, the discussion is made on the dependence of the decrease of Q on P_{gi}, from the viewpoint of the over-all thermal conductance U_o. For the discussion, ν is introduced to express the decrease of U_o, which is written as follows ;

$$\nu \equiv 1-U_o(\psi_2)/U_o(\psi_1) \ . \qquad (6-12)$$

The dependence of ν on P_{gi} is shown in Fig.6-10, where the solid curves represent the calculational ones. The calculational values of ν are obtained from the values of U_o calculated by Eqs.(6-10) and (6-11) using the values of n and P fitted in Fig.6-8 under each angle of inclination. As shown in Fig.6-10, ν has non-zero values in the region of P_{gi} between the sonic limit and the flat-front model conditions. Though there is no data in the region of P_{gi} below 10^{-2} Torr, ν in that region can be expected from the extrapolation of U_o by Eqs.(6-10) and (6-11). Table 6-1 shows the ν-values in the region of P_{gi} below 10^{-2} Torr, which are obtained from U_o extrapolated by Eqs.(6-10) and (6-11) using the values of n and P fitted in Fig.6-8 under each angle of inclination.

As revealed in this table, ν decreases and approaches zero with decreasing P_{gi}. Then it is said that ν has the zero value in the extremity of the sonic limit as well as in that of the flat-front model condition. Then it is said that the over-all thermal conductance U_o, though not influenced in these two extreme conditions, becomes sensitive to ψ in between. In the two extremities where $\nu=0$, the effect of gravity is completely compensated by the increase of the wick pumping pressure, however, the effect is partially compensated, depending on the value of ν, in between. The experimental results obtained in this chapter show that the thermal conductance of the heat pipe becomes sensitive to the variation of the body force acting on the liquid flow in the wick only when the small amount of non-condensable gas is present in the heat pipe.

The wick pumping pressure depends on radius r_e of the curvature at the vapor-liquid interface in the evaporator section. The change of radius r_e is caused by the difference of the mass flow rate between the vapor and the liquid flows, in the transient condition. Then, for a discussion of the change of the vapor flow resistance affecting the mass flow rate of vapor, the temperature distribution is examined under a different angle of inclination. Figure 6-11 shows the axial temperature distribution in a steady condition, with an inclination of 5 and 10 deg, at the same vapor temperature in the evaporator section, but at a different furnace temperature.

It is revealed in this figure that the sharp temperature gradient is decreased with an increasing angle of inclination. This suggests that the mixing of vapor and gas at the interface is increased. The increase of the vapor flow resistance due to the mixing of vapor and gas might influence the decrease of the heat transport rate, according to the change of ψ. However, a further discussion of any mixing phenomenon is beyond the scope of this thesis, and only the difference of the temperature distribution is pointed out here.

6-7 Concluding Remarks

The over-all thermal conductance of the heat pipe depends on the initial gas pressure. In the region of a high initial gas pressure, the thermal conductance can be described by the flat-front model but, with decreasing initial gas pressure, the thermal conductance deviates from the theoretical values obtained from the model and approaches that corresponding to the sonic vapor flow. In the transition region from the flat-front model condition to the sonic limit one, the thermal conductance becomes sensitive to the variation of the body force acting on the liquid flow in the wick, and the change of conductance depends on the initial gas pressure.

References

(1) Grover, G. M., Cotter, T. P. and Erickson, G. F. : J. Appl. Phys. 35, 1990 (1964).

(2) Cotter, T. P. : LA-DC-9026 (1967).

(3) Levy, E. K. : J. Eng. for Industry, Trans. ASME, (Nov. 1968).

(4) Kemme, J. E. : IEEE Transactions on Electron Devices, Vol. ED-16, No.8 (Aug. 1969).

(5) Foust, O. J. : Sodium-NaK Engineering Handbook, Vol.1.

(6) Marcus, B. D. : NASA CR-2018 (1972).

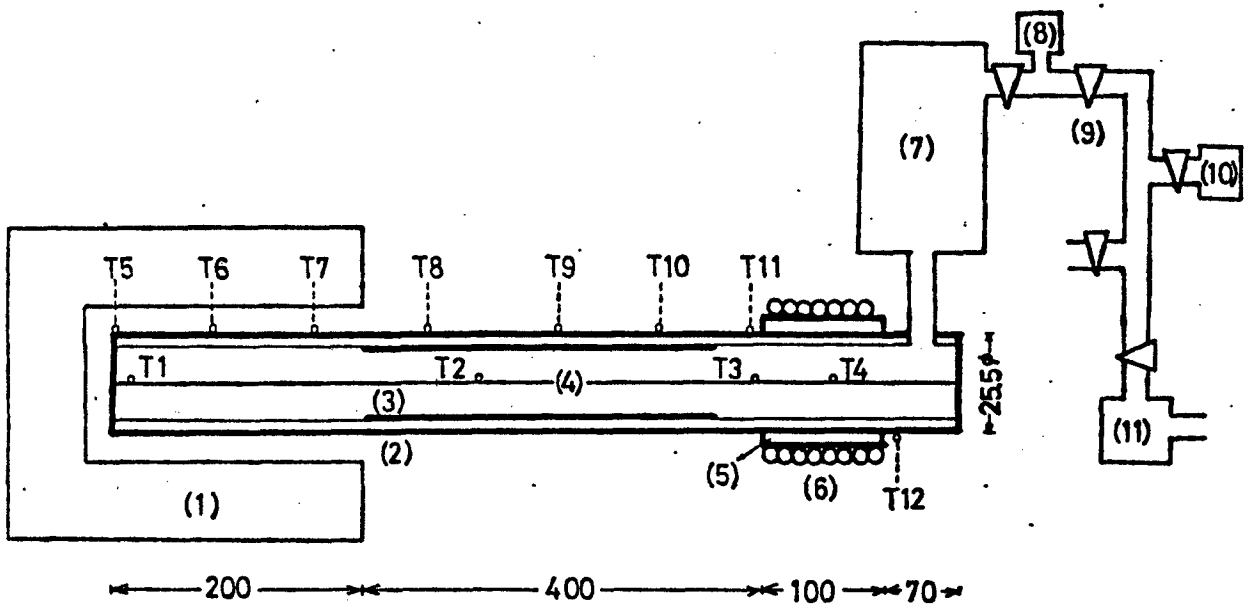

(1) Furnace
(2) Container
(3) Inner tube
(4) Thin rod
(5) Cooling jacket
(6) Cooling coil
(7) Gas reservoir
(8) Manometer
(9) Valve
(10) Argon bomb
(11) Vacuum system

Fig.6-1 Schematic diagram of potassium heat pipe and experimental apparatus

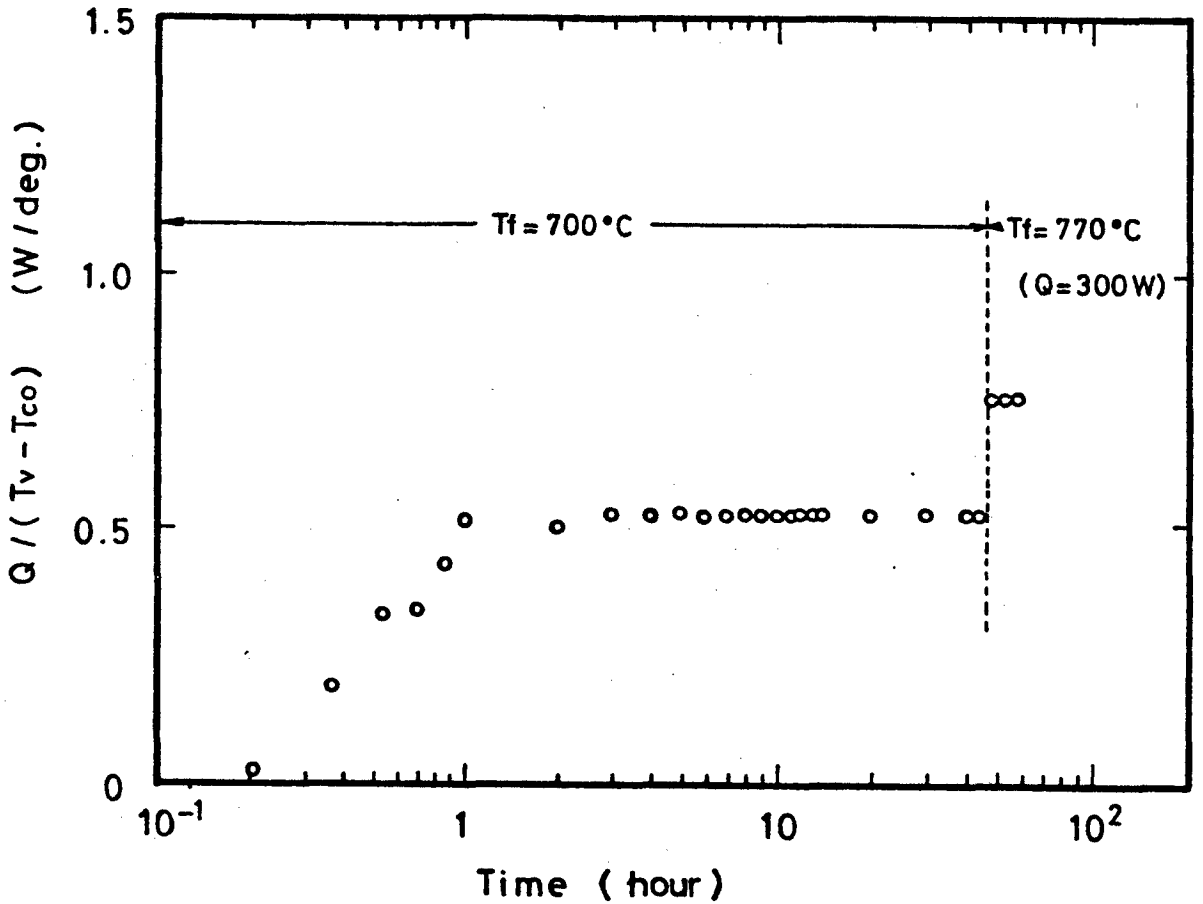

Fig.6-2 Transient behavior of potassium heat pipe without gas loading during trial run

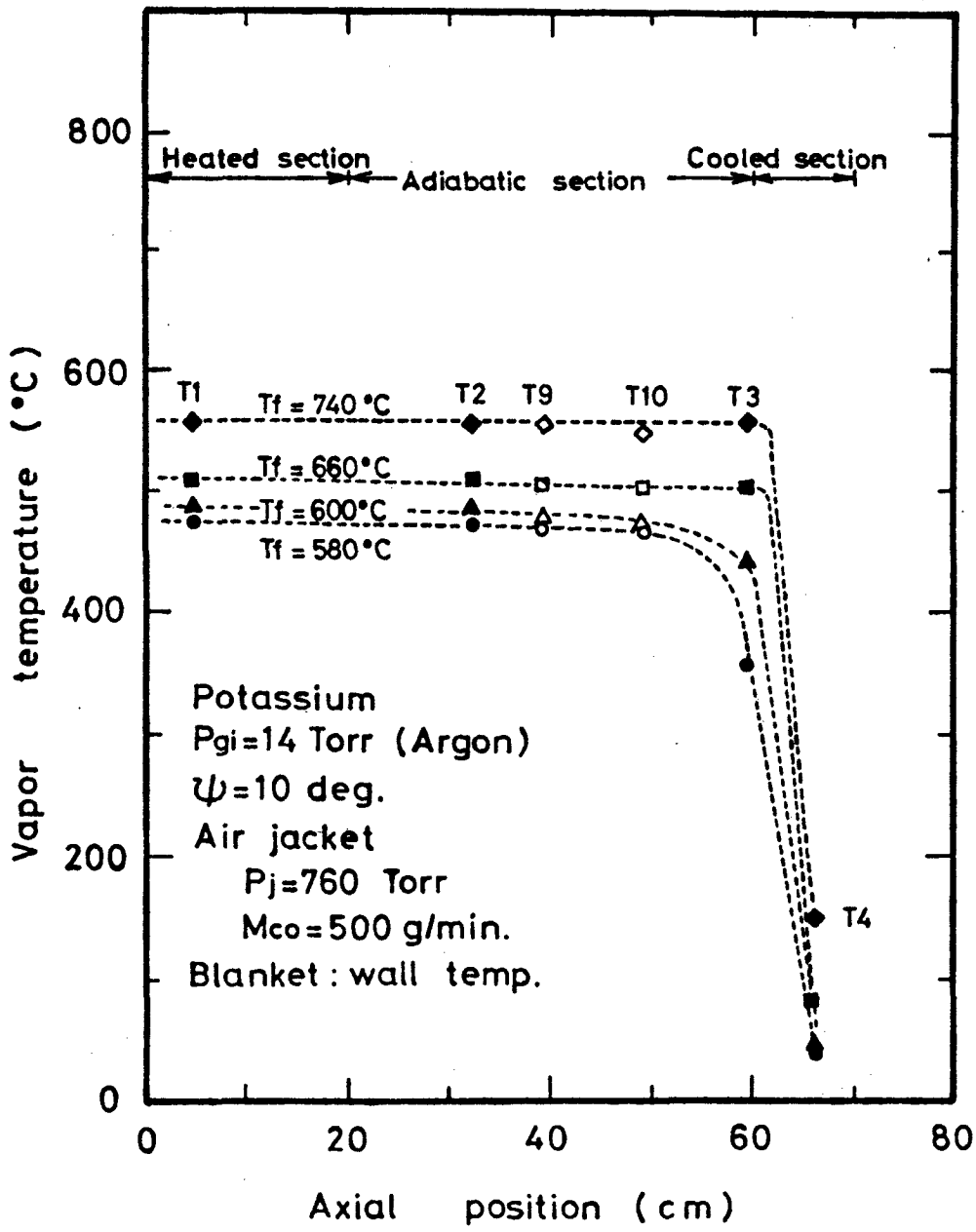

Fig.6-3 Axial temperature distribution of argon-loaded potassium heat pipe under various temperatures of furnace

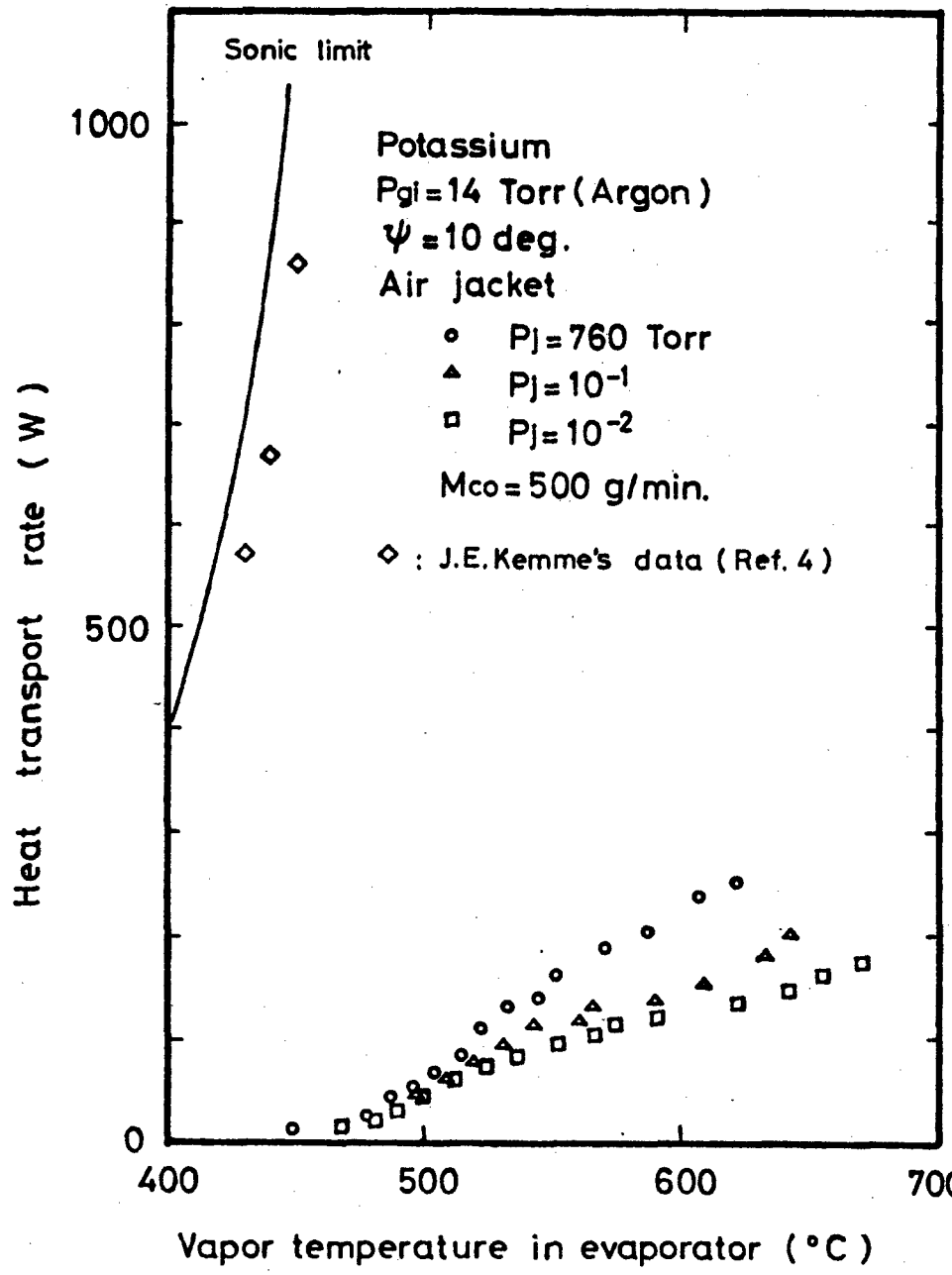

Fig.6-4 Q-T characteristics of argon-loaded potassium heat pipe

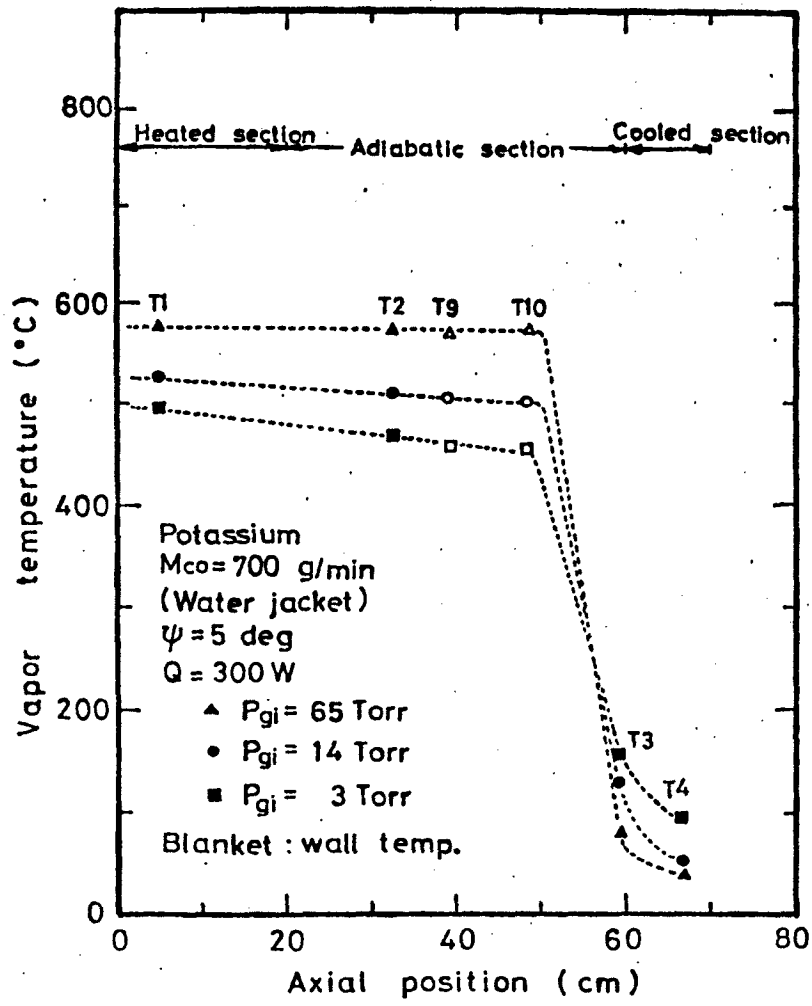

Fig.6-5 Axial temperature distribution at different initial gas pressure values

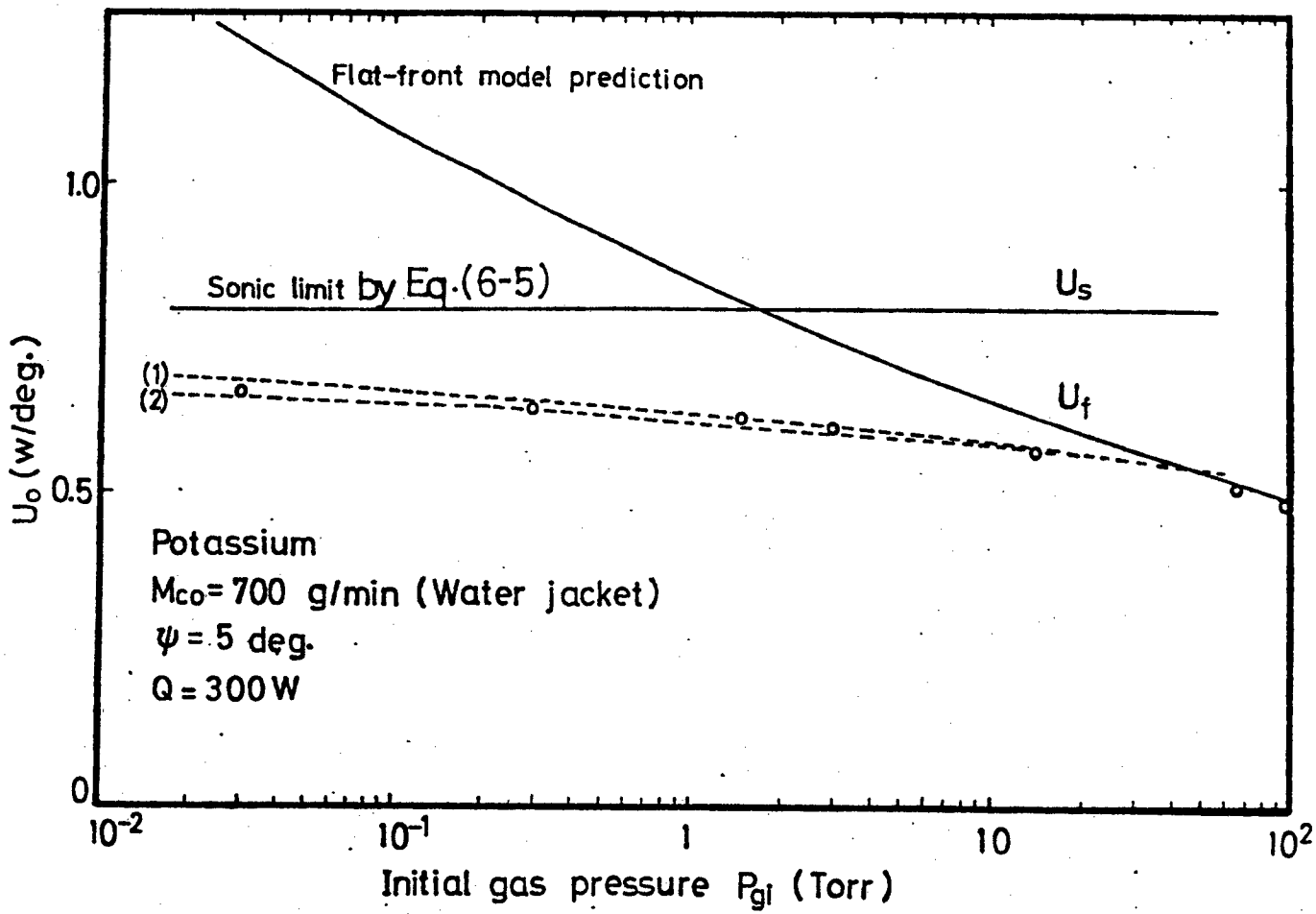

Fig.6-6 Dependence of U_o on P_{gi}

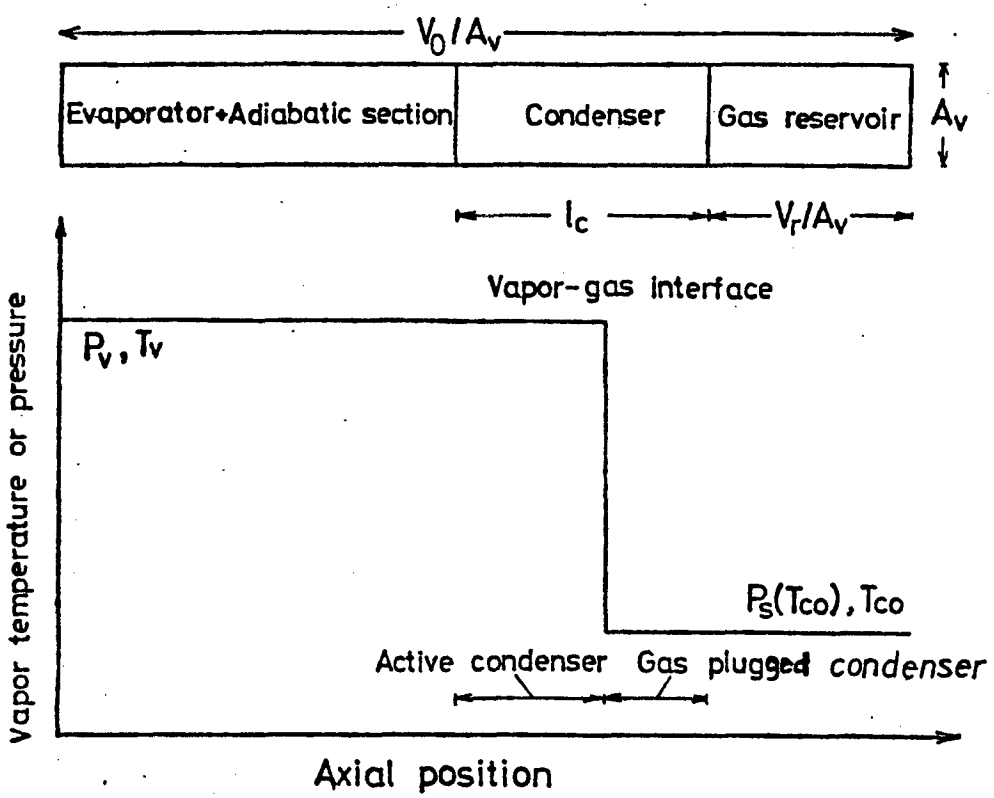

Fig.6-7 Schematic diagram of vapor temperature or pressure distribution in flat-front model

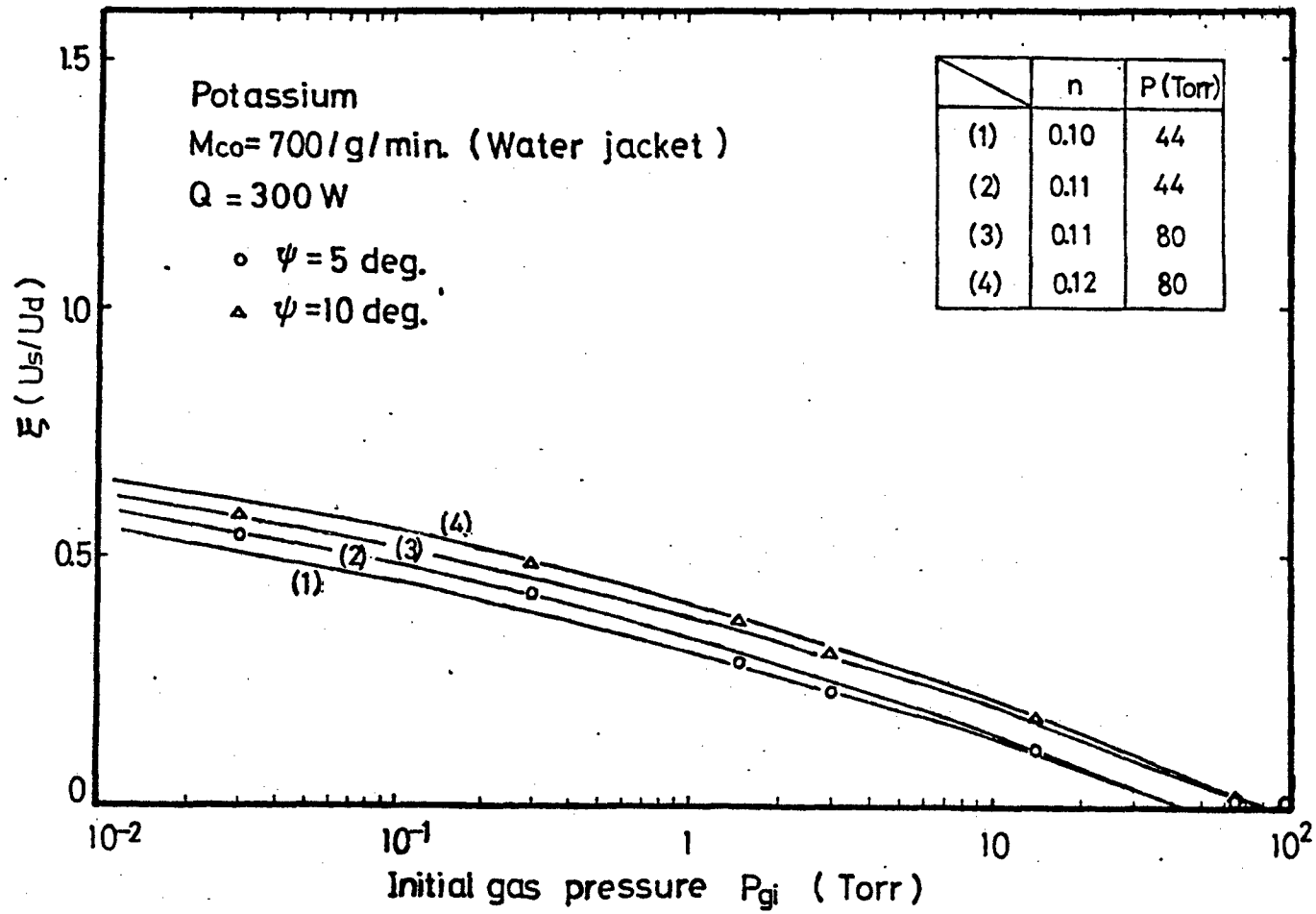

Fig.6-8 Dependence of ξ on P_{gi}

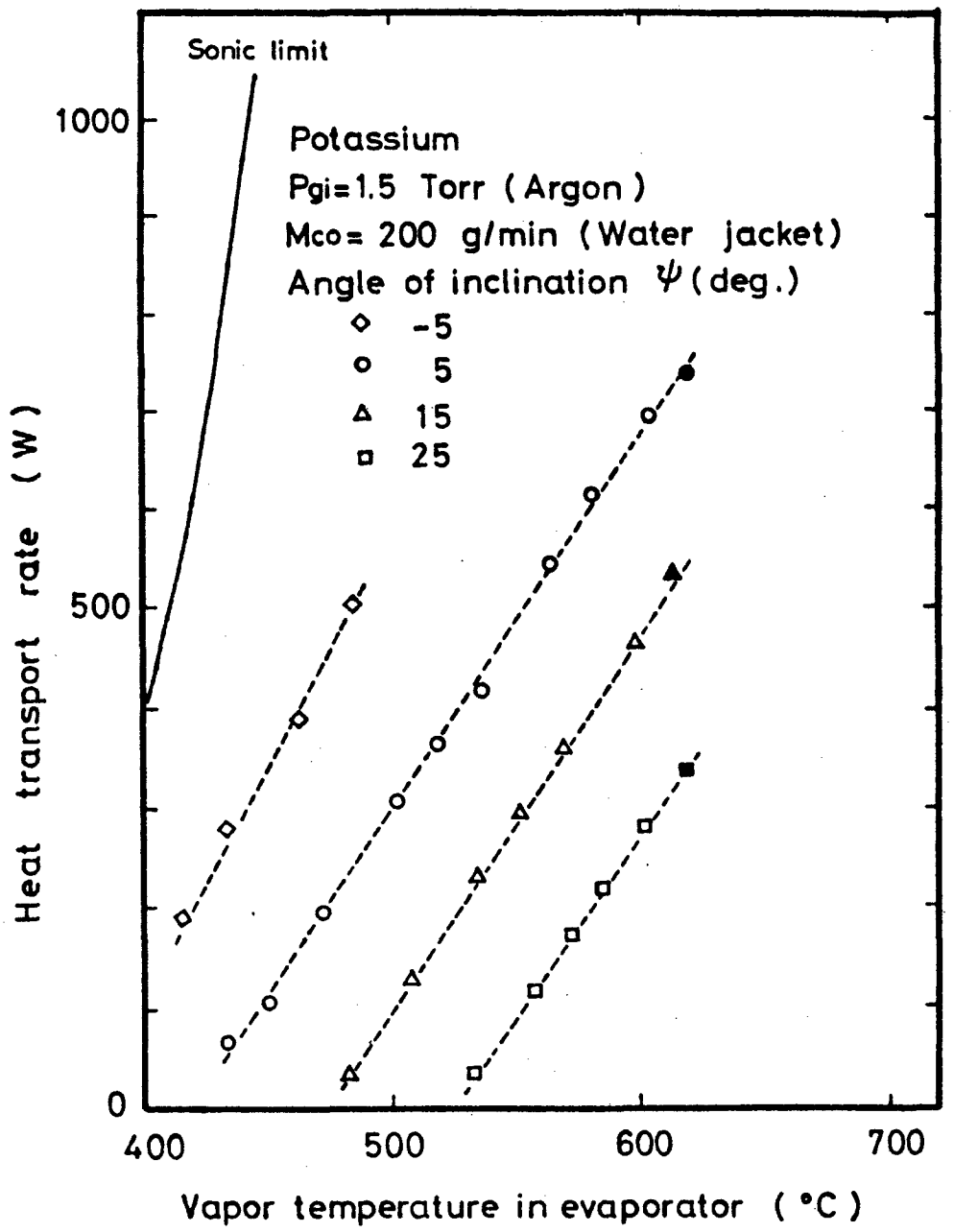

Fig.6-9 Q-T characteristics of argon-loaded potassium heat pipe under various angles of inclination

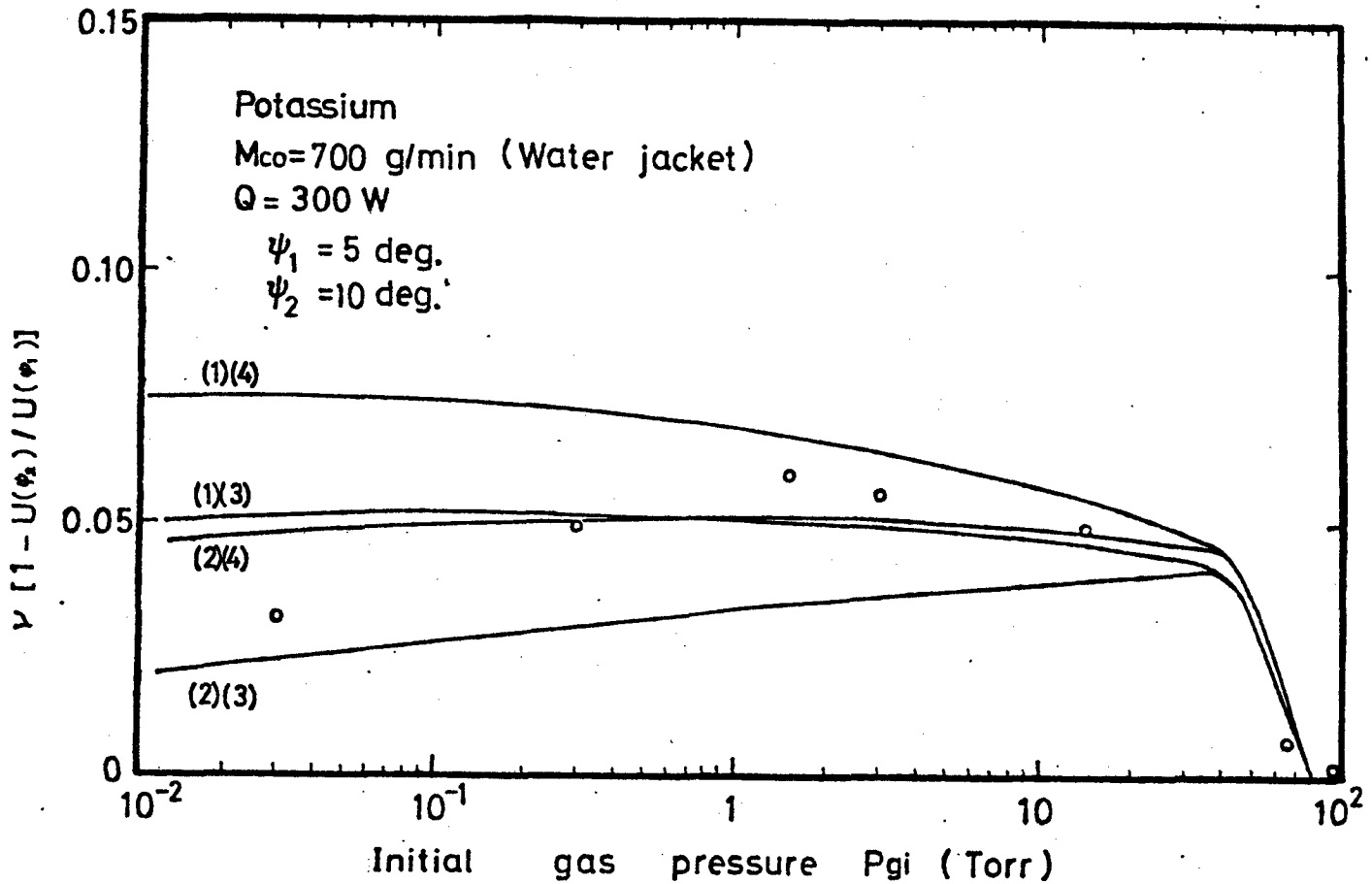

Fig.6-10 Dependence of ν on P_{gi}

Table 6-1 ν-values calculated by using the extrapolated U_o

P_{gi} (Torr)	(1), (4)	(1), (3)	(2), (3)	(2), (4)
10^{-2}	0.07	0.05	0.01	0.04
10^{-3}	0.07	0.05	0.01	0.04
10^{-4}	0.07	0.04	0.01	0.03
10^{-5}	0.05	0.03	0.00	0.02
10^{-6}	0.04	0.03	0.00	0.01

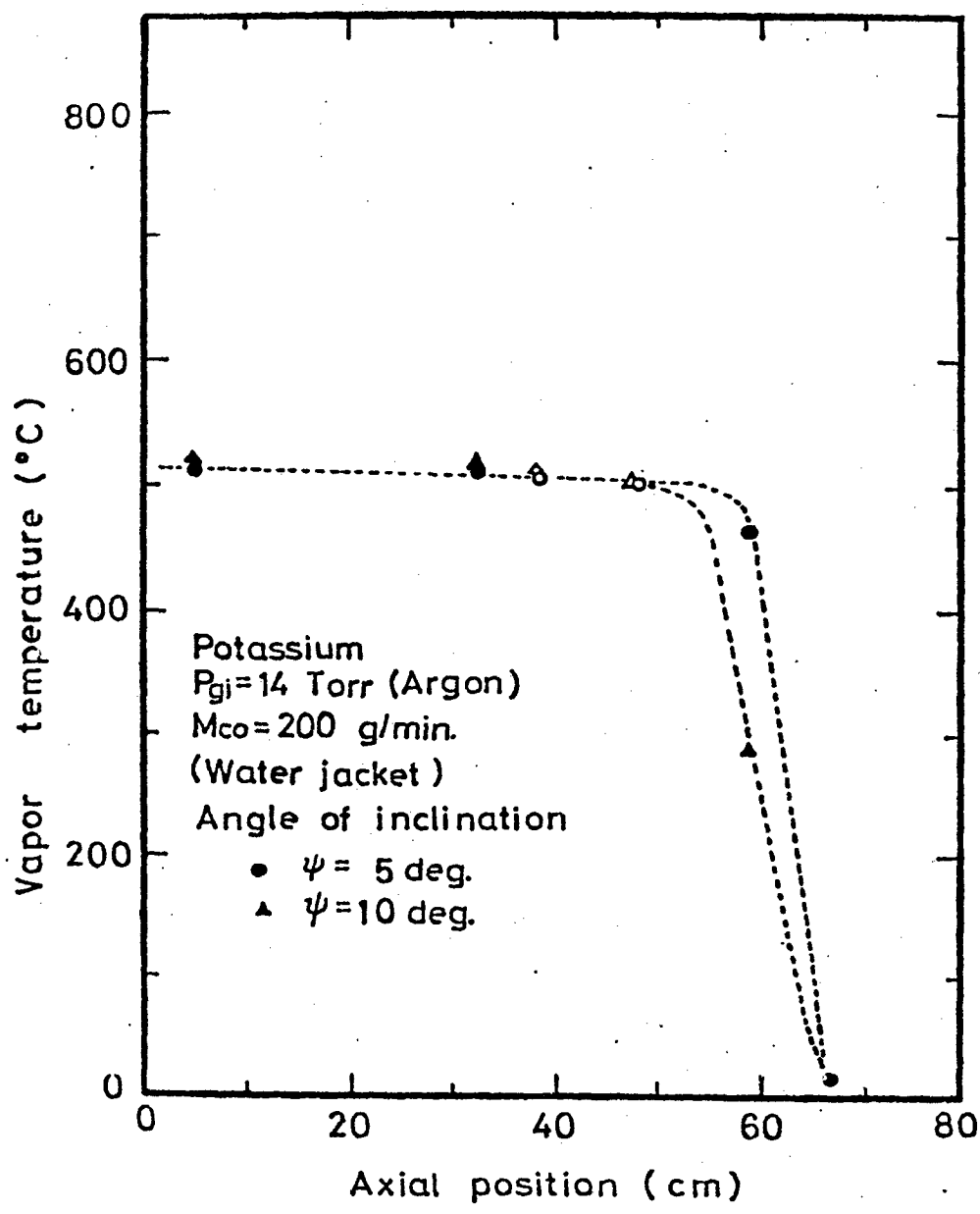

Fig.6-11 Comparison between axial temperature distribution of argon-loaded potassium heat pipe under different angles of inclination

Chapter 7.

Summary

The conclusions reached in the preceding chapters are summarized and discussed from an over-all point of view.

In Chapter 2, the heat transport equation of the heat pipe in the presence of the magnetic field is proposed, which is obtained from the viewpoint of the liquid flow in the wick on the basis of Darcy's law. The heat transport rate can be expressed in terms of latent heat, the wick pumping pressure, the over-all flow resistance for liquid and the increasing rate of flow resistance due to the MHD effect. The increasing rate depends on the Hartmann number of flow in the wick, which is defined by $\sqrt{\sigma_\ell B^2 K_\ell / \mu_\ell}$ from Darcy's law.

In Chapter 3, the influence of the magnetic field existing in the adiabatic section on the heat transport characteristics is experimentally studied with a potassium heat pipe. On applying the magnetic field, the heat transport rate decreases and the axial temperature distribution changes. It is concluded that the thermal conductance of the heat pipe depends on the MHD effect on the liquid flow in the wick. In this experiment, it is presumed that a small amount of non-condensable gas might be present in the heat pipe.

In Chapter 4, the Hartmann number of flow in the wick is estimated and the maximum heat transport rate limited by the maximum wick pumping pressure in the magnetic field is discussed. The Hartmann number increases with the increasing porosity of the wick as well as with the increasing field strength. The maximum heat transport rate decreases with increasing field strength, depending on the wick porosity.

In Chapter 5, the incipient boiling superheat of stagnant potassium is investigated and the discussion is made on the boiling limit in the magnetic field. The experimental results show that the incipient boiling superheat is not meaningfully influenced by the magnetic field. Nucleation in the wall cavity is not influenced by the MHD force which is negligible relative to the frictional force, hence the superheat is not influenced by the magnetic field. From the viewpoint of the incipient boiling superheat it is concluded that the boiling limit is not influenced by the magnetic field in the range of this experiment.

In Chapter 6, the influence of inert gas on heat transport characteristics of a potassium heat pipe with similar thermal performances is experimentally studied over a wide range of gas loaded, for further discussion of the experimental results described in Chapter 3. In the region of high initial gas pressure, the thermal conductance of the heat pipe can be described by the "flat-front" model but, with decreasing initial gas pressure, the thermal conductance deviates from the theoretical values obtained from the model and approaches that corresponding to the sonic vapor flow. In the transition from the flat-front model condition to the sonic limit one, the thermal conductance becomes sensitive to the variation of the body force acting on the liquid flow in the wick, and the change of the conductance depends on the initial gas pressure.

Summarizing the results mentioned above, an over-all view of the performance characteristics of the liquid metal heat pipe is discussed as follows.
The sonic limiting curve represents an ultimate limit which cannot be exceeded, regardless of wick structure. The sonic limit is independent of the body force acting on the liquid flow in the wick. Also, the boiling limit is not influenced by the magnetic field since the magnetic force is negligible compared with the frictional force within the nucleation cavity. On the other hand, the wick pumping limit depends greatly on the magnetic field strength and on the wick structure.

The entrainment limit is not investigated in the present thesis since the mechanism is not evident in detail, even in the absence of the magnetic field.

In the operating region under these limiting curves in Fig.1-1, the thermal conductance of the heat pipe depends on the amount of non-condensable gas. The thermal conductance becomes sensitive to the magnetic field only when a small amount of gas is present in the heat pipe. It should be mentioned here that in this experiment the liquid pressure drop is much greater than the vapor pressure drop. It can then be said that the liquid flow control by the magnetic field becomes possible when an appropriate amount of gas is present in a heat pipe with a dominant liquid pressure drop.

In the heat pipe application to the CTR blanket, not only the adiabatic section but also the evaporator and the condenser sections are in the magnetic field. For a general discussion of the heat transport characteristics of the heat pipe in the magnetic field it is necessary to know the influence of the magnetic field applied to each section of the heat pipe, one by one. In the present thesis, the influence of the magnetic field in the adiabatic section on the performance characteristics has been mainly studied. As for the influence of the magnetic field in the other sections, only the limit by the boiling initiation in the evaporator wick is discussed in Chapter 5 from the viewpoint of the incipient boiling superheat.

The influence of the magnetic field in the evaporator and the condenser sections on the heat transport characteristics will be the subject of a future study. In addition, it is mentioned that the adiabatic section of the heat pipe used in the present experiment is composed of a double-concentrated tube for perfect separation of the liquid flow from the vapor one. From a practical point of view, however, the adiabatic section might be composed of a single tube and then the interaction between the vapor and the liquid flows would affect the heat transport characteristics in the magnetic field. This is also the subject for a future study.

The other point left as a future problem is the phenomenon of mixing vapor and gas at the vapor-gas interface formed in the condenser section. This is of interest as a problem of basic physics.

Up to date, performance characteristics of liquid metal heat pipes in the magnetic field have been scarcely studied, though there are many problems still to be solved. Some of them are made clear in this thesis, and others are left for future studies. The investigations should be made step by step, the present thesis being the first step.

Acknowledgements

The author would like to express his gratitude to Professor T. Sano for his kindness and valuable suggestions.

The author wishes to express his thanks to Professor K. Sumita for his warm encouragement and helpful advice.

The author wishes to express his thanks to Professor S. Ishigai and Professor C. Yamanaka for their useful discussions.

In addition, the author wishes to thank Professor T. Sekiya and Professor S. Imoto for their encouragement.

The author is deeply indebted to Dr. Y. Fujii-e for his helpful advice and affectionate encouragement, without which this work could never have been accomplished.

The author is grateful to Dr. K. Miyazaki and Mr. S. Inoue for their warm encouragement and invaluable discussions.

The author is also grateful to Mr. N. Yamaoka, Mr. F. Manabe, Mr. M. Watari, Mr. H. Takatsu, Mr. M. Kawai and Mr. Y. Ieda for their technical assistance. And to the rest of the members of the Nuclear Power Research Group the author would like to express his appreciation.

List of Papers by the Author

(1) Influence of Magnetic Field on Boiling of Stagnant Potassium

J. Nucl. Sci. Technol., Vol.13, No.9 (Sept. 1976).

(2) Performance Characteristics of Potassium Heat Pipe Loaded with Argon.

J. Nucl. Sci. Technol., Vol.15, No.2 (Feb. 1978).

(3) Influence of a Transverse Magnetic Field on Heat Transport Characteristics of Potassium Heat Pipe.

J. Nucl. Sci. Technol., Vol.15, No. 10 (Oct. 1978).